Doctoral Thesis reviewed

by Ritsumeikan University

Segmental Bayesian estimation of model parameters from neuronal spike train data

(分割型ベイズ法による神経スパイクデータからの係数推定)

September, 2015

2015年9月

Doctoral Program in Integrated Science and Engineering

Graduate School of Science and Engineering

Ritsumeikan University

立命館大学大学院理工学研究科

総合理工学専攻博士課程後期課程

HOANG Thien Huu

ホアン　ティエン　フー

Supervisor: Professor TOKUDA Isao

研究指導教員: 徳田　功教授

"*If scientific analysis were conclusively to demonstrate certain claims in Buddhism to be false, then we must accept the findings of science and abandon those claims.*"

Tenzin Gyatso, The 14$^{\text{th}}$ Dalai Lama

To my beloved parents

Segmental Bayesian estimation of model parameters from neuronal spike train data

by

Hoang Thien Huu

Submitted to the Department of Mechanical Engineering
on June 30, 2015, in partial fulfillment of the
requirements for the degree of
Doctor of Philosophy

Abstract

Multi-electrode recording is now a common technique to simultaneously collect neuronal spike data of a population of the neurons in a brain region, and thus allows exploring various underlying functions of the brain. Computational modeling usually emerges when the parameters of interest can not be directly measured by the experiments. However, the inverse problem of estimating parameters from spike trains is severely ill-posed due to the huge mismatch in the system complexity between the brain and the model, and thus needs a stochastic approach to find most likely solutions among many possible ones. Since the brain typically exhibits complicated dynamics that is difficult for the model to reproduce, the modeling errors are inevitable. In the present thesis, we introduce a novel methodology based on the Bayesian inference framework to overcome that challenging issue. The experimental spike data is fractioned into short time segments and the model parameters are estimated segment by segment in the constraint that the segmental estimates are fluctuated around the neuronal estimates. By relaxing the parameter search, the segmental Bayes has been hypothesized to compensate the modeling errors and thus improve the estimation accuracy. The performance evaluation on experimental data indicated that the segmental Bayes outperforms the conventional Bayes and the minimum error method by minimizing the fitting errors in the feature space. It also had a strong robustness against non-stationarity of the spike data. To enable its further applications, verification of our proposed methods using simulation spike data was conducted. Unlike the experimental data, it is straightforward to measure the estimation errors because the true parameter values of the simulation data are known. Superiority of the segmental Bayes was also confirmed by the simulation data. We thus argue that the segmental Bayes provides a useful tool in neuroscience to estimate model parameters from spike trains with complicated dynamics.

Thesis Supervisor: Tokuda T. Isao
Title: Professor

Acknowledgments

First and foremost I would like to thank my advisor, Professor Isao T. Tokuda. It has been a great honor to be his very first Ph.D student. He has taught me, by an excellent example of his own works, how to become an independent researcher. His kindness and enthusiasm were always motivational for me even during tough times of my PhD pursuit. We have been working together for the last five years, and he has been very patient keeping me on track and putting things in the right place.

I would express my sincere thanks to Dr. Okito Yamashita, Dr. Masa-aki Sato, Professor Mitsuo Kawato and Professor Keisuke Toyama at the Advanced Telecommunications Research Institute (ATR). They are such wonderful researchers and warm-hearted mentors. I would never forget the joy we have had in the meetings organized every two weeks during my internship at ATR. I truly appreciate all their contributions of time and ideas to make my Ph.D experience productive and stimulating.

Members of the Rhythmic Systems Laboratory were greatly contributed to my personal and professional works at Ritsumeikan. I specially thank my current and former labmates. The lab has been a source of friendship as well as helpful assistance, particularly, in translating Japanese documents for me!

I gratefully acknowledge the funding sources that made my works possible. I was supported by the Society for the Advancement of Science and Technology at Ritsumeikan (ASTER) and the Japan Student Services Organization (JASSO) scholarships. The Japan Society for the Promotion of Science (JSPS) funded me a DC2 research fellowship and a Grant-in-Aids for research activities. My thanks also go to Ritsumeikan University for partially supporting the tuition fee of my Ph.D course.

Last but not least, I warmly thank my beloved family for encouraging my studies. Many thanks to my Vietnamese friends who shared with me lot of funny moments in our studentship.

September, 2015

Hoang Thien Huu

Ritsumeikan University

Contents

List of Figures

List of Tables

Chapter 1

Introduction

Over the past hundred years, biological research has gained a massive amount of knowledge about the structure and function of the brain. The core components in the nervous system are neurons, which are connected to each other to form neural networks. The neuronal signals consist of short electrical pulses, so-called action potentials or *spikes*, which are the elementary unit of signal transmission. The spikes can be observed by inserting a small electrode close to distinct parts – such as the soma, the dendrite or the spine – of a neuron. A spike train refers to a sequence of action potentials discharged by a neuron in regular or irregular patterns. The number and the timing of spikes are found very important in encoding information. Nowadays, multiple electrodes have become a standard tool in neuroscience research that enables simultaneous measurement of a population of neuronal activities in a brain region. Such measurement data provide important analysis challenges that must be resolved to understand the brain functions [10].

1.1 Parameter estimation in computational neuroscience

Because of the progress of theoretical neuroscience as well as the rapid growth of computer technology, computational modeling of the neuronal systems has been greatly

advanced these days. Highly developed measurement techniques in electrophysiology as well as in molecular biology enable agreement between experimental measurement and computational modeling even on a quantitative level [51, 48]. Still, the major difficulty lies in an imperfect measurement of the neuronal system. Namely, many of the dynamical variables hidden behind the observables as well as the parameter values that determine the neuronal circuitry cannot be properly measured. How to estimate such unknown variables and system parameters from the measured data, therefore, provides a big challenge in computational neuroscience [34, 57, 42, 55].

Modeling of the brain requires a number of parameters that are difficult to measure using current technology. Various approaches have been developed to resolve this "parameter estimation" problem. There are deterministic approaches that find unique solutions by optimization techniques, including the conjugate gradient, genetic algorithm, simulated annealing, and random search methods [71, 30, 31]. These methods are only applicable in relatively well-defined environments where the complexity of the system—such as the hierarchy, granularity, and degrees-of-freedom—is comparable between the model and experiment. Otherwise, parameter estimation problems become ill-posed. Another deterministic approach uses state and parameter reconstruction based on rather simplified neural models, such as Hindmarsh-Rose and FitzHugh-Nagumo models [69, 12]. Stochastic approaches were developed to overcome these difficulties, e.g., Markov random field model that estimates membrane resistance from the optical imaging data [33] and stochastic models that estimate the synaptic conductance from the electrophysiological recording data [6]. Nonlinear state space modeling has also been applied to estimate hidden dynamical variables as well as unknown parameters from the optical recording data [68, 45]. These approaches were also limited to the cases of a small mismatch between the model and experiment where the system complexity for the two cases was almost comparable.

Up to date, various techniques of parameter estimation have been applied to the computational modeling of the neural spiking data. The simplest approach is to define an error function, which measures the dissimilarity, in either timing or the feature extracted from the spike trains, between the experimental and simulated data, and

then to constraint the model parameters by minimizing the error [71, 1]. Alternative approach is to utilize multiple objective optimization that allows several error functions corresponding to different features of the spike data to be jointly employed and searches for the optimal trade-offs between them [11]. A state-space modeling has been also proposed to estimate the model parameters directly from the spike trains [38, 50, 47, 46]. In practical situations, however, these approaches have a severe limitation, because of (1) non-stationarity of the measured data and (2) imperfectness of the computational model. In the parameter estimation, it is usually assumed that the parameter values do not change in time and that the time series measured from the system is stationary. In many systems, however, it is typically that the parameter values such as the conductance values change slowly in time due to their plasticity. For high-dimensional complex systems, non-stationary dynamics such as intermittent switching among quasi-attractors is observed quite often [21, 25, 66, 67]. Concerning the model selection, it is usually that the computational model has less complexity in neuronal circuitry and much less number of neurons compared to the real network of neurons. The parameters should be therefore estimated under the condition that the data is non-stationary and that the model is an imperfect representation of the experiment. These difficulties inevitably cause modeling errors and thus cause inaccurate solutions of the inverse problem for estimating model parameters from the spike data.

To deal with such difficulties, this thesis develops a new methodology based on hierarchical Bayes, which performs Bayesian estimation of the parameters in two steps. Our idea is to suppose that, in the non-stationary data, the parameter values can change from one time-segment to another. Accordingly, the spike data are divided into short time-segments, within which the data can be considered stationary. In the first step, the parameters are estimated to each time-segment of individual neurons, allowing the parameter values to be varied in time. This relaxes the condition of the parameter search. In the second step, a single set of parameter values is estimated to the entire time-segments of individual neurons with a constrained condition. The segmental Bayes is equivalent to the method used in the recent studies that introduced

the system noise in order to reduce the estimation errors due to modeling errors [24, 20, 3]. To allow segmental fluctuations in the parameter estimates and to merge the estimates for a single neuron imply to assume noise for parameter estimation with the constraint to minimize fluctuations within single neurons. We show that this step-wise procedure is quite effective for non-stationary spiking data even when the model is imperfect.

1.2 Modeling of the network of inferior olive neurons

As a target system of our computation modeling, we focus on a network of inferior olive (IO) neurons, which play a central role in the cerebellar learning [44, 2, 23, 27, 28]. It has been widely accepted that the cerebellar learning takes place at the Purkinje cells (PCs), which output motor commands to the cerebellar nuclei (CN) while receiving two types of major excitatory inputs: nearly 100,000 parallel fibers from granule cells and a sole but powerful climbing fiber input from IOs [53, 70]. Whereas the granule cells transmit signals from the sensory system and the cerebral cortex, the IO neurons were reported to send error signals [14, 32]. When conjointly activated at the PCs, these two inputs cause a long-term depression (LTD), reducing the efficacy of the synaptic transmission in the parallel fiber [22]. One of the remaining issues on the cerebellar learning is the low firing rate of the IO neurons with typically a single or two spikes per movement. This provides a severe limit for the IO neurons to precisely transmit the error signals with a high temporal resolution.

Concerning this problem, the network effect of the IO neurons should be taken into account. As far as the IO neurons are activated in a synchronous manner, ensemble of IO neurons behaves as a single neuron, which does not help to overcome the limited capability of the error transmission. However, if the IO neurons operate asynchronously, the spike timings of each neuron are scattered to increase the time resolution of the population coding of the error signal. Here, it is natural to consider that the electrical coupling regulates the level of synchrony between the IO neurons. If the coupling strength is too strong, it induces coherent IO activities. If

the coupling is too weak, on the other hand, common input stimuli entrain the IO cells, resulting again in their coherent activities. In contrast, intermediate strength of the electrical coupling was found to induce irregular or even chaotic spikes, which effectively desynchronize the IO activities and thus optimize the population coding [58, 63, 29]. Since optimal learning is realized with an intermediate coupling strength that maximizes the level of the chaotic activity, this hypothesis has been termed as *chaotic resonance*.

To examine the chaotic resonance hypothesis, it is indispensable to estimate the coupling strength from the spiking data of the PCs, since its direct measurement is not possible. Two types of conductance mainly contribute to the electrical coupling between the IO neurons. The first one is the gap-junctions [62, 40, 41], whereas the second one is the inhibitory conductance. Recent experiments have suggested that the coupling strength is adjusted by the release of GABAergic inhibition from deep cerebellar nuclei (DCN) in a form of glomerulus structure [7]. Indeed, the effect of the two conductances on the IO neurons have been confirmed by the injection of GABA blocker picrotoxin (PIX) as well as by the injection of gap-junction blocker carbenoxolone (CBX). After the PIX injection, the firing rate and the synchrony of the IO activity were increased, while, conversely, the CBX reduces them [37, 36, 9].

The aim of the present study is to estimate the gap-junctional (g_c) and inhibitory (g_i) conductances from spike trains of real neurons under PIX, CBX, and control (CON) conditions. To deal with the non-stationary data inherent in the spiking activity of the PCs, the segmental Bayes was applied for the parameter estimation. Our methodology was evaluated by studying the effect of the CBX, which should directly decrease the gap-junctional conductance, and that of the PIX, which should decrease the inhibitory conductance as a GABA antagonist. Our results indeed showed that the CBX decreased 10% g_c from CON level, whereas PIX reduced 80% of g_i. These results support the hypothesis that inhibitory input from DCN is a reasonable mechanism to control oscillatory and synchronous IO activity.

1.3 Organization of the thesis

Alongside the **Introduction**, the thesis is organized in other five chapters as follows.

- The methodology of our studies is described in **Chapter 2**, which contains detailed descriptions of the neuronal network model and the proposed approaches to estimate two model parameters from spike train data.

- **Chapter 3** shows analytic results of the simulation data, which was used to construct the forward model of the Bayes framework. We confirm that the simulation model can reliably reproduce the firing dynamics of the experimental data despite the imperfectness of the model.

- To confirm the usability, validation of those approaches using the simulation data is developed in **Chapter 4**. Unlike the experimental data, the underlying conductance values are known for the simulation data, which are thus suitable for the validation purpose. Performance evaluation on the simulation data strongly confirmed the superiority of the segmental Bayes.

- In **Chapter 5**, we provide quantitative measurements of the two parameters of interest for experimental spike data collected in [37, 36, 9]. Three estimation methods – including the segmental Bayes, the non-segmental Bayes and the minimum error method – were performed. The segmental Bayes has been shown to outperform two comparative methods by minimizing the fitting error between experimental and simulation data in the feature space. It also has a potential to overcome the highly non-stationary firing dynamics of the experimental data.

- Finally, we summarize the methodology, main findings, important contributions as well as future works of our studies in **Chapter 6**.

Chapter 2

Methodology

Advanced measurement technologies in neuroscience enable the collection of a massive amount of neuronal data. Nevertheless, exploring the underlying functional mechanisms is a very hard task. For instance, given measured spike trains of a population of neurons, it is not trivial to understand how the neurons electrically interact with each other to induce synchronized or irregular firing patterns. Although mathematical modeling of the brain provides a plausible solution, it usually faces two challenges. First, the model should be constructed in a way that it is not only consistent with the anatomy of the neuronal network, but also capable of reproducing the quantitative dynamics of the brain. Second, an effective method for fitting the simulated spike data to the experimental data is strongly required. In this chapter, we propose a novel methodology to resolve those two challenges.

The aim of our study is to estimate gap-junctional (g_c) and inhibitory (g_i) conductance from the spike data of inferior olive (IO) neurons. Since these two parameters are at a synapse level, we constructed an IO network model of nine detailed neurons, each of which consist of three Hodgkin–Huxley-type compartments. Because of the complexity of the real IO network, we, however, cannot expect that the model can perfectly reproduce the observed experimental data and there is no simple one-to-one mapping between the experimental data and the model parameters. Apparently, the deterministic algorithms that find a unique solution are not well suited to the parameter estimation problem.

In [49], we adopted a deterministic approach, so called minimum-error method, to find optimal parameter values that generate the best simulation results with a minimum distance in the feature space to the experimental data. The reason why this deterministic algorithm worked moderately well is because it follows stochastic characteristics. Experimental data set from different neurons were divided into short time segments, and the parameters were estimated for each segment. Then, the distribution of the estimated parameter values from all segments and neurons was treated as a population. This introduces a source of stochastic natures. The minimum-error method can be interpreted as an extreme case of a class of stochastic Bayesian estimation algorithm where variance of the forward models is assumed infinitely small. However, assuming an infinitely small variance in the forward models is not theoretically validated and full development of a stochastic Bayesian framework for a broad range of parameter estimation problems is desirable.

In a recent study [18], we introduced a theoretical framework of Bayesian estimation which estimates parameter values for segments using the forward models generalized to the entire spike data and merges the segmental estimates into a single estimate for every neuron in the basis of neuronal constraint. This constraint avoids over-fitting of the forward models to experimental data, reducing the number of Gaussians by three orders of magnitude, and the fitting errors to less than one-third of those in the minimum-error method with highly non-stationary data.

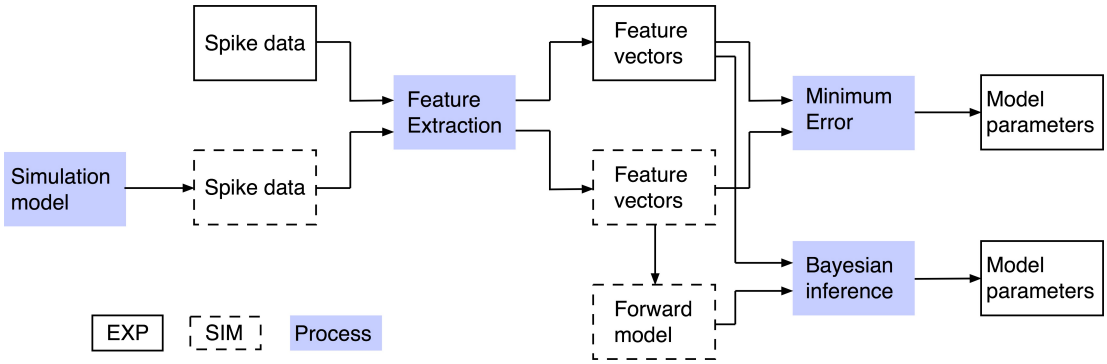

Figure 2-1: Flowchart of the parameter estimation approaches

2.1 The simulation network model

2.1.1 The IO model

A conductance-based model of IO neurons, which consists of a soma, dendrite and spine compartments, was developed in our studies. We extended the model proposed in an earlier study [58] by adding the spine compartment to account for the electrically coupling between two IO neurons via gap-junctions (Figure 2-2A). The somatic compartment contains ionic channel conductances for the inward sodium current (g_{Na}), the delayed rectifier outward potassium current (g_K), the low-threshold calcium current (g_{Cal}), the anomalous inward rectifier current (g_h), and the leakage current (g_o). The dendritic compartment includes ionic channel conductances for the high-threshold calcium current (g_{Cah}), the calcium-activated potassium current (g_{Kca}), and the leakage current (g_d). The spine compartment includes a conductance for a leakage current (g_p). All three classes of compartment receive a total of 260 excitatory (g_e) and inhibitory (g_i) synaptic conductances driven by Poisson noise generators. All of the ionic, crosstalk, and synaptic conductances are defined for a unit surface area of the soma, dendrite, or spine membrane.

The electrophysiological properties of the IO model also depend on the crosstalk conductances between the soma and dendrite compartments ($g_{od/do}$) and between the dendrite and spine compartments ($g_{dp/pd}$) (Figure 2-2B). They are defined per membrane surface area and therefore depend on neuron morphology: the ratio of the somatic area to the total surface area (p), and the ratio of the area of the four spines to the total surface area (q) (cf. Equations (A.9), (A.13), (A.14) and (A.17)).

2.1.2 The network structure

The network model consisted of 3×3 array of IO neurons, each of which was mutually connected to its four neighboring neurons (Figure 2-2C) by a gap junction from one of its spines to one of its neighbor's represented by the gap-junctional conductance (g_c) (Figure 2-2B). Several studies have shown that IO neurons covey heterogeneity in

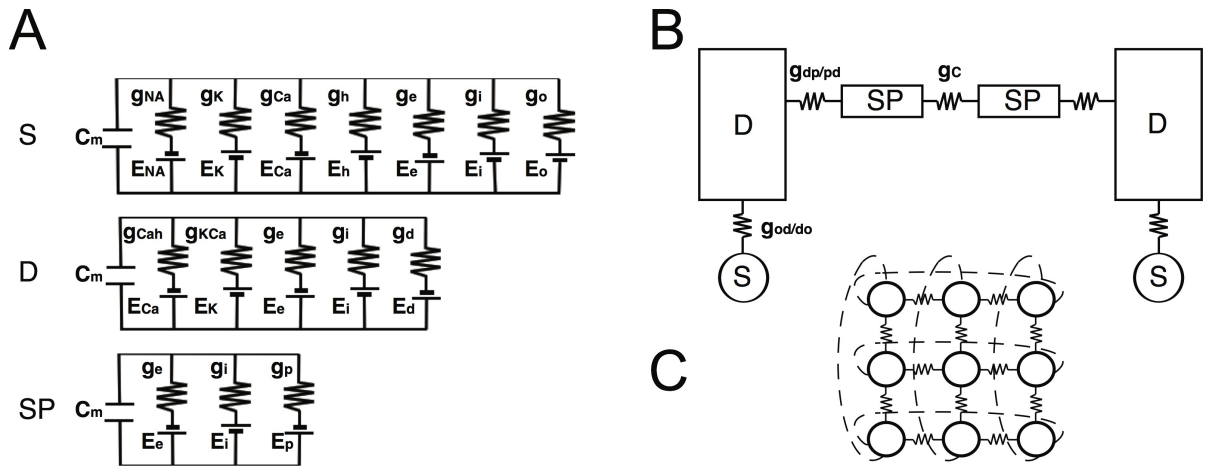

Figure 2-2: The IO network model
A-C: a schematic diagram of the IO network model consisting of 3×3 neurons, each of which consists of the soma (S), dendrite (D) and spine compartments (SP). The S, D and SP compartments contain five, three and one ionic channels defined by the modified Hodgkin-Huxley equations (cf. Equations A.1–A.17, Appendix A) and the excitatory and inhibitory input conductance (g_e and g_i). Two neighboring neurons are coupled via gap junctional conductance (g_c) and axial spine conductance ($g_{dp/pd}$).

their membrane conductance [43, 65, 19]. In our model, most conductance parameters were shared for the IO neuron population except the maximal conductance of the low threshold calcium g_{Cal} and the coupling strength g_c to account for the variability in the neuronal properties. We assumed comparable variations of g_{Cal} and g_c, sampling them from uniform distributions with the maximum deviation set at 5% of the mean.

2.1.3 Simulation of the spike data by the network model

We computed the electrical activity in each compartment of the model with step-wise variations of the gap-junctional conductance (g_c) and the inhibitory conductance (g_i). The other model parameters including the crosstalk conductances were fixed to the values essentially the same as those used by [58, 49] at the values shown in Table A.1. The electrical activity in each compartment of the model was simulated with interactions through a system of ordinary differential equations that determines the changes of the membrane potential within the somatic, dendritic, and four spine

compartments.

We simulated the membrane potential time courses of the nine cells with stepwise changes of the two model parameters, i.e., inhibitory synaptic conductance g_i, and coupling conductance g_c were varied in the range of [0–1.5 mS/cm^2] and [0–2.0 mS/cm^2], respectively, with an increment of 0.05 mS/cm^2, whereas the excitatory conductance g_e was fixed at 0.03 mS/cm^2. We generated a total of $31 \times 41 = 1271$ sets of 5000 s long SIM spike trains. Within these spike trains, the time of each spike was defined as the time when the change in the somatic membrane potential exceeded 20 V/s. The numerical integration of the system of ordinary differential equations was executed by the CVODE package (part of the SUNDIALS package) with 0.5 ms time steps. For numerically stiff problems like the present IO network model, CVODE includes backward differentiation formulas.

2.2 Parameter estimation from spike data

Our estimation techniques can be classified as a feature-based approach, in which the spike data is characterized by multiple features. For the minimum error method, the model parameter is determined by the closest distance between the experimental and simulation data in the feature space. For the Bayesian approach, the forward model is constructed based on feature vectors of the SIM data to estimate the *likelihood* distribution and then the *posterior* probability is inferred follows the Bayes theorem. In this section, we describe how to characterize spatiotemporal features from the spike data as well as the construction of the forward model. Next, the Bayesian inference and the minimum error methods were proposed to estimate two model parameters from the extracted features. Finally, we briefly compare those two methods in the view point of probability theory.

2.2.1 Feature extraction from spike data

First of all, the feature vectors were extracted from the spike train data. To deal with non-stationarity, we divided the spike train of each neuron, for both experimental and

simulated data, into 50-second time-segments. For each segment, sixty-eight features were computed to characterize spatiotemporal dynamics of the IO firing. All features were evaluated by the mutual information and only top twenty-five informative ones, which convey highest information about the parameter space, were selected. Principal component analysis (PCA) was conducted to further reduce the redundancy of those twenty-five features, and top three principal components, which amount up to 55% of the data variance, were used for estimating the model parameters.

Spatiotemporal features of the spike data

A total of sixty-eight features – including firing frequency, local variation, auto-correlation, cross-correlation, minimal distance and spike distance – were extracted from the spike data. The first three classes of the feature vector (FV) represent temporal properties, while the last three represent spatial properties of the firing patterns.

1. The mean firing rate (FR) of spike segments was calculated as the number of spikes in 1s.

2. The local variation (LV) was calculated as

$$LV = \frac{1}{R-1}\sum_{r=1}^{R-1}\frac{3(T_{r+1}-T_r)^2}{(T_{r+1}+T_r)^2} \tag{2.1}$$

   where $T_r(r = 1, 2...R)$ is the r-th inter-spike interval (ISI) [61].

3. The auto-correlogram for 20 delays (ACG 1-20) ranged from 0-1000ms with a bin size of 50ms.

$$ACG_{x,i}(\tau) = \sum_{k=1}^{K} x_i(t_k)x_i(t_k-\tau) \tag{2.2}$$

   where $x_i(t_k)$ represents the occurrence of spikes at the k-th time step in i-th neuron and τ is the time delay.

4. The cross-correlogram for 20 delays (CCG 1-20) corresponding to delays of 0-

50ms, 50-100ms, ... 950-1000ms were computed as:

$$CCG_{x,i,j}(\tau) = \sum_{k=1}^{K} x_i(t_k)x_j(t_k - \tau) \tag{2.3}$$

5. The minimal distance [16] (MD1-25) was defined as a normalized distribution of

$$s_l^{i,j} = 1 - \exp\left(\frac{-2\min_m |t_l^i - t_m^j|}{\bar{d}_j}\right) \tag{2.4}$$

between the l-th spike of neuron i and a spike of neuron j. Here, t_l^i is the time of l-th spike of the neuron i, $\bar{d}_j$ is the mean ISI of the j-th neuron, and m ranged from 1 to the total number of spikes of neuron j. If the spike train is generated by a random process, the distribution will be uniformly distributed between 0 and 1.

6. The spike distance [35] (SD) was defined as

$$D_S = \frac{1}{T}\int_{t=0}^{T} S(t)\mathrm{d}t \tag{2.5}$$

where $S(t)$ are instantaneous dissimilarity values derived from differences between the spike times of the two spike trains and T is the recording time. SD is bounded in the range [0,1] with the value zero obtained for perfectly identical spike trains.

Feature selection by mutual information

For effective estimation of the parameters, only the main features that contain rich information on g_i and g_c were selected according to the mutual information (MI) between the FV and the conductance values.

We let $g = (g_i, g_c) \in G$ as a pair of the conductance parameters and $x \in X$ denote one component of the FV. Then, the MI that represents the amount of information

of G conveyed by x was computed as:

$$I(G;x) = \sum_{g \in G} P(x,g) \log \left(\frac{P(x,g)}{P(x)P(g)} \right) = \sum_{g \in G} P(x|g)P(g) \log \left(\frac{P(x|g)}{P(x)} \right) \tag{2.6}$$

Here, the conditional distribution $P(x|g)$ was approximated as a histogram of x given a pair of (g_i, g_c), the distribution $P(x)$ was assumed to be a histogram of x, and $P(g)$ was assumed to be a uniform distribution. The sixty-eight FVs were rated by the MI and top twenty-five FVs were selected for principal component analysis.

Principal component analysis

The principal component analysis (PCA) was conducted as a solution to the following equation:

$$(\boldsymbol{X}^T \boldsymbol{X})\boldsymbol{W} = \boldsymbol{\lambda}\boldsymbol{W} \tag{2.7}$$

where $(\boldsymbol{X}^T \boldsymbol{X})$ is the covariance matrix of the twenty-five features of EXP spike data $\boldsymbol{X}$. We used a Statistical Toolbox (MATLAB) to calculate the eigenvector $\boldsymbol{W}$ and eigenvalues $\boldsymbol{\lambda}$. The principal component vector $\boldsymbol{Y}$ was computed as the linear transformation of the feature vector $\boldsymbol{X}$ as follows:

$$\boldsymbol{Y} = \boldsymbol{X}\boldsymbol{W} \tag{2.8}$$

The top three principal components of $\boldsymbol{Y}$ were selected according to the highest eigenvalues (0.27, 0.21 and 0.09) for construction of the forward model.

2.2.2 Forward model

To evaluate the fitting between the experimental and simulation data, we constructed a forward model as a likelihood function in PCA space using the simulation data. The likelihood function at each grid point of $g = (g_i, g_c)$ was approximated by a mixture of Gaussians:

$$P(y|g) = \sum_{k=1}^{K} \pi_k N(\mu_k, \Sigma_k) \tag{2.9}$$

where $N(\mu, \Sigma)$ is the multivariate Normal (Gaussian) distribution with mean μ and covariance Σ. The number of components K, mixing coefficients π_k, means μ_k and covariance matrices Σ_k of Gaussian mixtures were estimated from the simulated data for a given parameter set g using the variational Bayes algorithm [8, 56]. The average number of component K, which was automatically determined by the algorithm, was 8.55. Figure 2-3 shows a scatter plot of the SIM data at $(g_i, g_c) = (0.7, 0.7)$ and a mixture of Gaussians that fit SIM data in the 2-dimensional PCA space.

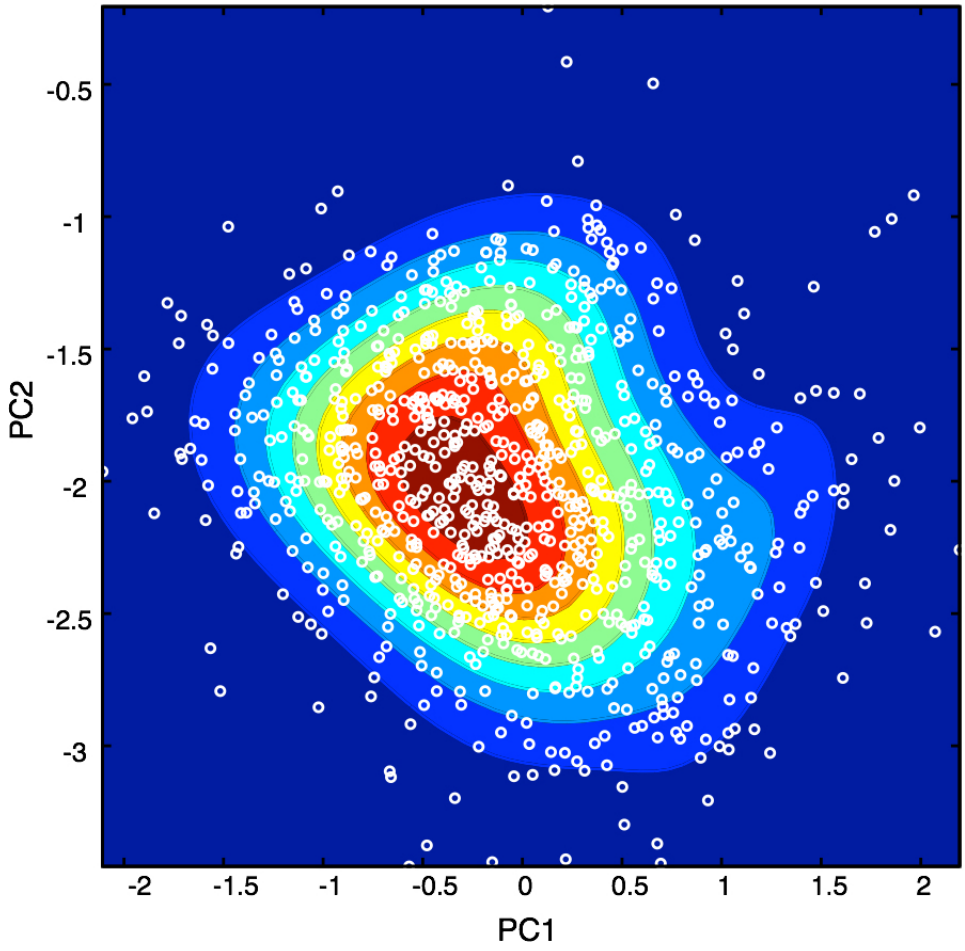

Figure 2-3: An example of the SIM spike data and its fitted mixture of Gaussians Scatter plot of the SIM spike data at $(g_i, g_c) = (0.7, 0.7)$ in the 2-dimensional PCA space (white circles) and a mixture of Gaussians (contour plot) that fit the SIM data as the likelihood function at that point.

The performance of the fitting was confirmed by comparing the PC scores of SIM with that predicted by the forward model by the 3-dimensional statistical energy test

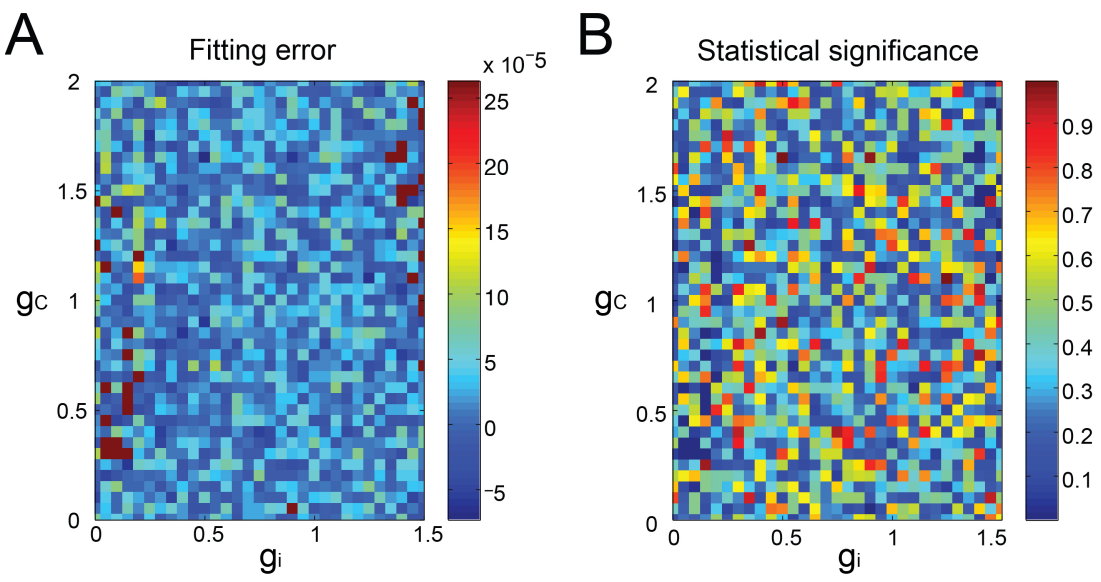

Figure 2-4: Goodness of fit of the forward model to the SIM spike data
A: 3-dimensional pseudo-color representation of the fitting error of the forward model estimated as the energy test statistics between the predictions of the forward model and the SIM data plotted for g_i and g_c. B: statistical significance of the error.

[4]. It is worth noting that minimum energy method is binning-free and thus feasible in multi-dimensional applications. In general, the match was acceptable (Figure 2-4A), with the statistical difference being not significant ($p > 0.1$) for most combinations of g_i and g_c, except for few ones (about 2%) where the statistical significance was rather high ($p < 0.03$) (Figure 2-4B).

2.2.3 The Bayesian method

Our goal is to estimate the parameter $g = (g_i, g_c)$ from an experimental feature vector y, thus it can be regarded as an inverse problem. By utilizing the Bayes rule, the posterior probability $P(g|y)$ is proportional to the product of the likelihood and the prior probability of a parameter set:

$$P(g|y) \propto P(y|g)P(g) \tag{2.10}$$

with the likelihood $P(y|g)$ was approximated as in Equation 2.9 and the prior probability $P(g)$ was uniformly distributed.

The novel point of our proposed framework is an introduction of the commonality and neuronal constraints. The former constraint was based on the fact that PIX and CBX selectively reduce g_i and g_c, respectively. This implies that g_c remains unchanged between the PIX and CON conditions, whereas g_i is identical between the CBX and CON conditions. The commonality constraint thus assumes that PIX and CON data share the same conductance value for g_c in a prior distribution, while CBX and CON data share the same g_i. The latter constraint dealt with the estimation errors caused by the modeling errors. To minimize such errors, we divided the spike data of each neuron into small time-segments, applied the Bayesian inference to estimate g_i and g_c for every segment, and then merged the segmental estimates into a single estimate for each neuron.

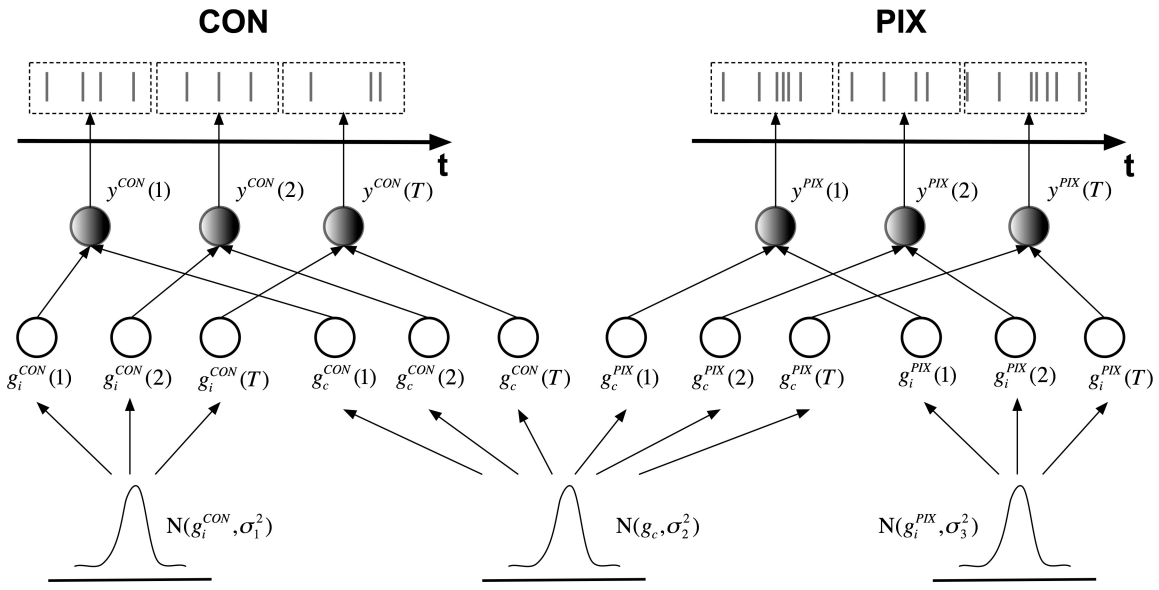

Figure 2-5: A schematic diagram of the segmental Bayesian inference.

Figure 2-5 illustrates how the Bayes framework incorporates those two constraints as estimating two model parameters for a representative neuron in the CON and PIX conditions. Under the assumption of commonality constraints, g_c values of PIX and CON data are drawn from a unique *Gaussian* distribution $N(g_c, \sigma_2^2)$ with the mean

g_c and variance σ_2^2, whereas the g_i values of those two conditions separately fluctuate around two *Gaussian* distributions $N(g_i^{CON}, \sigma_1^2)$ and $N(g_i^{PIX}, \sigma_3^2)$. The variations in the conductance parameters are considered to reflect discrepancies between the simulation dynamics and the complex dynamics of real neurons. The Bayes estimation for neurons in the CON and CBX conditions is similar, with the shared g_i and independent g_c values. In the following subsections, we explicitly describe details of the hierarchical Bayesian framework with the neuronal and commonality constraints.

Bayesian model with the commonality constraint

We let $y^{CON}(t)$ and $\boldsymbol{y^{CON}} = \left[y^{CON}(1), y^{CON}(2), \ldots, y^{CON}(T)\right]$ denote the feature vector for time segment t and the collection of the segment-wise feature vectors for the control conditions, respectively. Similarly $y^{pha}(t)$ and $\boldsymbol{y^{pha}}$ were defined for the pharmacological condition, where pha stands for either PIX or CBX. In addition, we let $\left[g_i^{CON}, g_c^{CON}, g_i^{pha}, g_c^{pha}\right]$ denote the conductance parameters for a neuron under the control and pharmacological conditions.

Thus, the likelihood function of the model is

$$\begin{aligned} P\left(\boldsymbol{y^{CON}}, \boldsymbol{y^{pha}} \middle| g_i^{CON}, g_c^{CON}, g_i^{pha}, g_c^{pha}\right) \\ &= P\left(\boldsymbol{y^{CON}} \middle| g_i^{CON}, g_c^{CON}\right) P\left(\boldsymbol{y^{pha}} \middle| g_i^{pha}, g_c^{pha}\right) \\ &= \prod_t P\left(y^{CON}(t) \middle| g_i^{CON}, g_c^{CON}\right) P\left(y^{pha}(t) \middle| g_i^{pha}, g_c^{pha}\right), \end{aligned} \tag{2.11}$$

where $P(y|g_i, g_c)$ is the probability density function constructed from the forward model. As prior distributions, we assume uniform distributions for g_i and g_c with commonality constraints. In the case of $pha = PIX$, $g_c^{CON} = g_c^{PIX}$, thus

$$\begin{aligned} P_0\left(g_i^{CON}, g_c^{CON}, g_i^{pha}, g_c^{pha}\right) \\ &= P_0\left(g_i^{CON}, g_i^{PIX}, g_c^{CON}\right) \delta\left(g_c^{CON} - g_c^{PIX}\right) \propto \delta\left(g_c^{CON} - g_c^{PIX}\right) \end{aligned} \tag{2.12}$$

where $\delta(g_c)$ is the Dirac delta function. In the case of $pha = CBX$

$$P_0\left(g_i^{CON}, g_c^{CON}, g_i^{pha}, g_c^{pha}\right) = P_0\left(g_c^{CON}, g_c^{CBX}, g_i^{CON}\right)\delta\left(g_i^{CON} - g_i^{CBX}\right) \propto \delta\left(g_i^{CON} - g_i^{CBX}\right) \quad (2.13)$$

Equations (2.11), (2.12) or (2.11), (2.13) constituted the neuronal Bayesian model.

Hierarchical Bayesian model with the neuronal and commonality constraints

The idea of neuronal constraint can be implemented by expanding the Bayesian model to a hierarchical one that employs an additional hierarchical prior distribution for merging the segmental estimates. In this model, each segment data is generated from a segment-wise conductance parameters $\left[g_i^{CON}(t), g_c^{CON}(t), g_i^{pha}(t), g_c^{pha}(t)\right]$ which vary around neuronal conductance parameters $\left[g_i^{CON}, g_c^{CON}, g_i^{pha}, g_c^{pha}\right]$.

Thus, the likelihood function became

$$\begin{aligned} &P\left(\boldsymbol{y^{CON}}, \boldsymbol{y^{pha}} \middle| g_i^{CON}(1:T), g_c^{CON}(1:T), g_i^{pha}(1:T), g_c^{pha}(1:T)\right) \\ &= P\left(\boldsymbol{y^{CON}} \middle| g_i^{CON}(1:T), g_c^{CON}(1:T)\right) P\left(\boldsymbol{y^{pha}} \middle| g_i^{pha}(1:T), g_c^{pha}(1:T)\right) \\ &= \prod_t P\left(y^{CON}(t) \middle| g_i^{CON}(t), g_c^{CON}(t)\right) P\left(y^{pha}(t) \middle| g_i^{pha}(t), g_c^{pha}(t)\right) \end{aligned} \quad (2.14)$$

, where $g_i^{CON}(1:T) = \left[g_i^{CON}(1), g_i^{CON}(2), \ldots, g_i^{CON}(T)\right]$ are collections of the segment-wise conductance, and similarly, for $g_c^{CON}(1:T)$, $g_i^{pha}(1:T)$ and $g_c^{pha}(1:T)$.

We assume segment-wise conductance parameters vary around neuronal conductance parameters following Gaussian distribution with unknown variance parameters. Thus, the prior distribution became

$$P\left(g_i^{CON}(1:T), g_c^{CON}(1:T), g_i^{pha}(1:T), g_c^{pha}(1:T) \middle| g_i^{CON}, g_c^{CON}, g_i^{pha}, g_c^{pha}\right) = \prod_t P\left(g_i^{CON}(t), g_c^{CON}(t), g_i^{pha}(t), g_c^{pha}(t) \middle| g_i^{CON}, g_c^{CON}, g_i^{pha}, g_c^{pha}\right) \quad (2.15)$$

$$
\begin{aligned}
&P\left(g_i^{CON}(t), g_c^{CON}(t), g_i^{pha}(t), g_c^{pha}(t) \middle| g_i^{CON}, g_c^{CON}, g_i^{pha}, g_c^{pha}\right) \\
&= \begin{cases} N\left(\begin{bmatrix} g_i^{CON} & g_c^{CON} \end{bmatrix}, \begin{bmatrix} \sigma_1 & 0 \\ 0 & \sigma_2 \end{bmatrix}\right) N\left(\begin{bmatrix} g_i^{PIX} & g_c^{PIX} \end{bmatrix}, \begin{bmatrix} \sigma_3 & 0 \\ 0 & \sigma_2 \end{bmatrix}\right) & \text{if } pha = PIX \\ N\left(\begin{bmatrix} g_i^{CON} & g_c^{CON} \end{bmatrix}, \begin{bmatrix} \sigma_1 & 0 \\ 0 & \sigma_2 \end{bmatrix}\right) N\left(\begin{bmatrix} g_i^{CBX} & g_c^{CBX} \end{bmatrix}, \begin{bmatrix} \sigma_1 & 0 \\ 0 & \sigma_3 \end{bmatrix}\right) & \text{if } pha = CBX \end{cases}
\end{aligned} \tag{2.16}
$$

Under the assumption of commonality constraints, g_c distributions of PIX and CON shared the same variance σ_2, and g_i distributions of CBX and CON shared the unique variance σ_1 (Equation 2.16). Equations (2.14), (2.15), (2.16) constitute the segment-wise neuronal Bayesian model, which has hierarchical prior distributions.

Finally the commonality priors as given by (2.12) or (2.13) are assumed in the hyper-prior distribution. Note that this model is equivalent to the neuronal Bayesian model (Equations (2.11), (2.12) or (2.11), (2.13)) above when all σ_1, σ_2 and σ_3 are fixed to zeros.

Inference of conductance parameters and variance parameters

Given the variance parameters, the conductance values can be inferred by computing the posterior distribution of the hierarchical Bayesian model above. The posterior distribution for the four conductance parameters for a neuron is given as:

$$
\begin{aligned}
&P\left(g_i^{CON}, g_c^{CON}, g_i^{pha}, g_c^{pha} \middle| \boldsymbol{y^{CON}}, \boldsymbol{y^{pha}}\right) \\
&\quad = \frac{P\left(\boldsymbol{y^{CON}}, \boldsymbol{y^{pha}} \middle| g_i^{CON}, g_c^{CON}, g_i^{pha}, g_c^{pha}\right) P0\left(g_i^{CON}, g_c^{CON}, g_i^{pha}, g_c^{pha}\right)}{P\left(\boldsymbol{y^{CON}}, \boldsymbol{y^{pha}}\right)}
\end{aligned} \tag{2.17}
$$

Here, the numerator, the likelihood distribution integrated across all segments, is

given by:

$$
\begin{aligned}
&P\left(\boldsymbol{y^{CON}}, \boldsymbol{y^{pha}} \middle| g_i^{CON}, g_c^{CON}, g_i^{pha}, g_c^{pha}\right) \\
&= \int\int\int\int P\left(\boldsymbol{y^{CON}}, \boldsymbol{y^{pha}} \middle| g_i^{CON}(1:T), g_c^{CON}(1:T), g_i^{pha}(1:T), g_c^{pha}(1:T)\right) \\
&\quad P\left(g_i^{CON}(1:T), g_c^{CON}(1:T), g_i^{pha}(1:T), g_c^{pha}(1:T) \middle| g_i^{CON}, g_c^{CON}, g_i^{pha}, g_c^{pha}\right) \\
&\quad \mathrm{d}g_i^{CON}(1:T), \mathrm{d}g_c^{CON}(1:T), \mathrm{d}g_i^{pha}(1:T), \mathrm{d}g_c^{pha}(1:T)
\end{aligned}
\tag{2.18}
$$

and the denominator, called the model evidence, is given by:

$$
\begin{aligned}
P\left(\boldsymbol{y^{CON}}, \boldsymbol{y^{pha}}\right) = \int\int\int\int &P\left(\boldsymbol{y^{CON}}, \boldsymbol{y^{pha}} \middle| g_i^{CON}, g_c^{CON}, g_i^{pha}, g_c^{pha}\right) \\
&P_0\left(g_i^{CON}, g_c^{CON}, g_i^{pha}, g_c^{pha}\right) \mathrm{d}g_i^{CON}, \mathrm{d}g_c^{CON}, \mathrm{d}g_i^{pha}, \mathrm{d}g_c^{pha}
\end{aligned}
\tag{2.19}
$$

In general, these integrals are very difficult to evaluate. However, since in our problem, the domain of (g_i, g_c) is discretized with bins of 0.05 and the probability mass is assumed on the grid points, the integrals appearing in Equations (2.18), (2.19) are replaced by summation and can be numerically evaluated without difficulty. Here, the conductance parameters are estimated as the maximizer of the posterior distribution.

Inference of the variance parameters

The variance parameters were adjusted based on the model evidence value $P\left(\boldsymbol{y^{CON}}, \boldsymbol{y^{pha}}\right)$ for each neuron. We discretized the space of the possible variance parameters with a bin size of 0.025 and computed the evidence (Equation 2.19) for all the combinations of σ_1, σ_2 and σ_3, then selected those that maximized the model evidence value.

2.2.4 The minimum error method

As a solution to the inverse problem of estimating g_c and g_i from test data, we searched for values of g_c and g_i, the corresponding training data of which showed the closest

match (minimum PCA distance) to the test data in the PCA space. The distance between the two data sets is defined as

$$distance(y, \hat{y}) = \sqrt{\sum_{i=1}^{N} (y_i - \hat{y}_i)^2} \tag{2.20}$$

where y and $\hat{y}$ represent PCA scores of the training and test data, respectively, and $N = 3$ is the number of the selected PCA components.

For the aforementioned commonality constraint, in [49] we developed the "juggling algorithm" in which the match between the SIM and EXP spike segments was searched under the constraint that g_c and g_i remain unaffected by PIX and CBX administration, respectively. In other words, g_c and g_i should agree with each other between CON and PIX conditions and between CON and CBX conditions, respectively.

2.2.5 Differences between those two methods

Here, we briefly explain the main differences in our two proposed approaches in a view of the probability theory [49, 18]. In the minimum-error method, the parameter estimation for an experimental spike train in a short time segment was given a best fit by $g = (g_i, g_c)$ with which the error between the experimental and simulation data in PCA space was minimal over all of the generated simulation data. From the Bayesian viewpoint, this can be interpreted as a maximum likelihood estimation with the following Gaussian mixture likelihood function $P(y|g)$:

$$P(y|g) = \sum_{n=1}^{N_s} \frac{1}{N_s} N(y_n(g), \sigma^2 I) \approx C \exp\left(-\frac{1}{2\sigma^2} \min_n (y - y_n(g))^2\right) \tag{2.21}$$

where $y_n(g)$ is the n-th simulation sample at (g_i, g_c), N_s is the total number of simulation samples (n = 12,600) at (g_i, g_c) and C is the normalization constant. Here, the variance σ^2 is assumed to be infinitesimally small. This forward model highly depends on the generated simulation data and tends to over-fit the experimental data. The average component number K for the Bayes inference was roughly three

orders of magnitude smaller than that for the minimum-error algorithm (8.55:12,600), indicating the existence of this over-fitting in the latter case. Thus, the Bayesian method prevents over-fitting by explicitly estimating the smooth likelihood function using an optimal number of Gaussian mixtures.

Alternatively, in [49], the commonality constraint was imposed at the condition level rather than the neuronal level. Specifically, it was assumed that PIX and CON data share the same g_c, whereas CBX and CON data share the same g_i across the whole data set including different animals. In the Bayesian method, we assumed a more biologically reasonable commonality constraint at the neuronal level: (g_i, g_c) in different time segments were common for each neuron and the PIX and CON data share the same g_c, whereas CBX and CON data share the same g_i for each neuron.

2.3 Data analysis

2.3.1 Sensitivity analysis of feature vectors

Sensitivity analysis was conducted to evaluate how the FVs sense g_i and g_c as the partial differential of FV with respect to the g_i and g_c, e.g., $\frac{\partial FV}{\partial g_i}$ and $\frac{\partial FV}{\partial g_c}$. We constructed a 3-dimensional map for each FV as a function of g_i and g_c, by normalizing FV by the peak value. The sensitivity was determined as the mean of the partial differentials across the entire range of g_i or g_c.

2.3.2 Non-stationary analysis

We evaluated the non-stationarity of IO firing dynamics by three measures, including LV (cf. Equation (2.1)), Kolmogorov-Smirnov (KS) distance of the inter-spike intervals (ISIs) to the Poisson model, and the standard deviation of the firing frequency.

Chapter 3

Results: Analysis of the model

Construction of the simulation model is a very first step in any estimation techniques. The model is desired to be capable of capturing complicated dynamics of the brain. However, because of huge differences in the complexity between the model and the brain, such as the number of neurons as well as the connectivity among them, the modeling error is inevitable. The question of how to evaluate the complicated firing dynamics to quantify the fitting of the simulation spike data to the experimental one is thus critical and challenging. To answer that question, we analyze the spike data in terms of the feature vectors described in the section 2.2.1, which includes the following three steps: 1) sixty-eight features were extracted from the spike data, 2) we selected twenty-five features conveyed rich information about the parameter space, and 3) principal component analysis was conducted for those selected features. We show that, within such feature space, simulation spike data can perfectly cover experimental spike data collected from various experiments. Analytic results in this chapter confirm that our developed simulation model can reliably reproduce the firing dynamics of IO neurons, and it is thus suitable for the estimation problem.

3.1 Feature estimation of the simulation data

Firstly, we tentatively extracted sixty-eight FVs—including FR, LV, SD, ACGs, CCGs and MDs—from the simulation spike data. Figure 3-1 shows the feature maps of

five major features for all combinations of g_i and g_c. We selected the delay time for ACG and CCG around their oscillatory peaks, which may represent the time courses of auto- and cross-interaction within and across the cells (ACG1, 50ms; CCG1, 50ms; etc.). Sensitivity analysis indicated that some FVs (ACG1, FR, LV) were only sensitive to g_i, whereas others (MD2 and CCG1) were sensitive to both g_i and g_c. This is probably due to the fact that g_i controls the firing in individual cells, while g_c controls the interaction across neurons. The results indicate that FVs convey variable information concerning g_i and g_c, and we need to select only those conveying significant information concerning g_i and g_c for construction of the forward model, eliminating those conveying poor information.

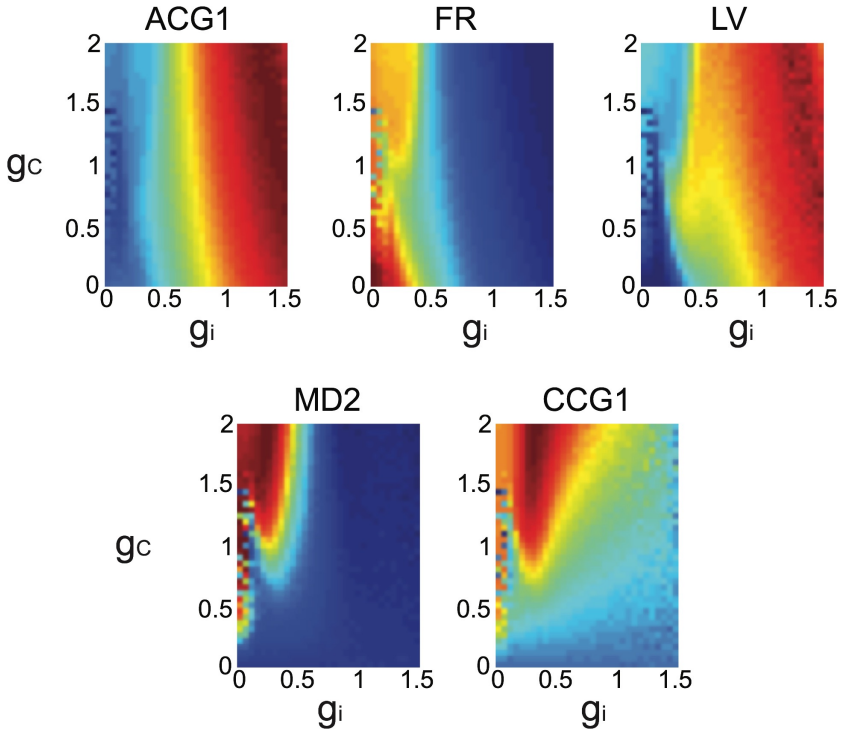

Figure 3-1: Maps of five major features for g_i and g_c
3-dimensional maps of the five representative FVs (ACG1, FR, MD2, LV, CCG1) plotting the mean of FVs for g_i and g_c by pseudo-color representation. The color-map is normalized by the peak values.

3.2 Mutual information

Next, we performed the mutual information (MI) analysis concerning g_i and g_c to select the FVs (Figure 3-2 and Table 3.1). ACG1 conveyed the highest information (1.76 bits) and FR the next highest (1.41), whereas MD2, LV, and CCG1 conveyed rather small information (0.89, 0.56 and 0.34 bits, respectively). ACG1 is most informative of g_i, because it focused on the first peak of ACG oscillation, and ACG2, ACG3, ACG4 are less informative because they are off-focused from the first peak. g_i influences the time course of the after-hyperpolarization and rebound depolarization, acting as the shunting conductance to these membrane potential changes. Therefore, those focused on the ACG peaks are more informative of g_i than the off-focused ones.

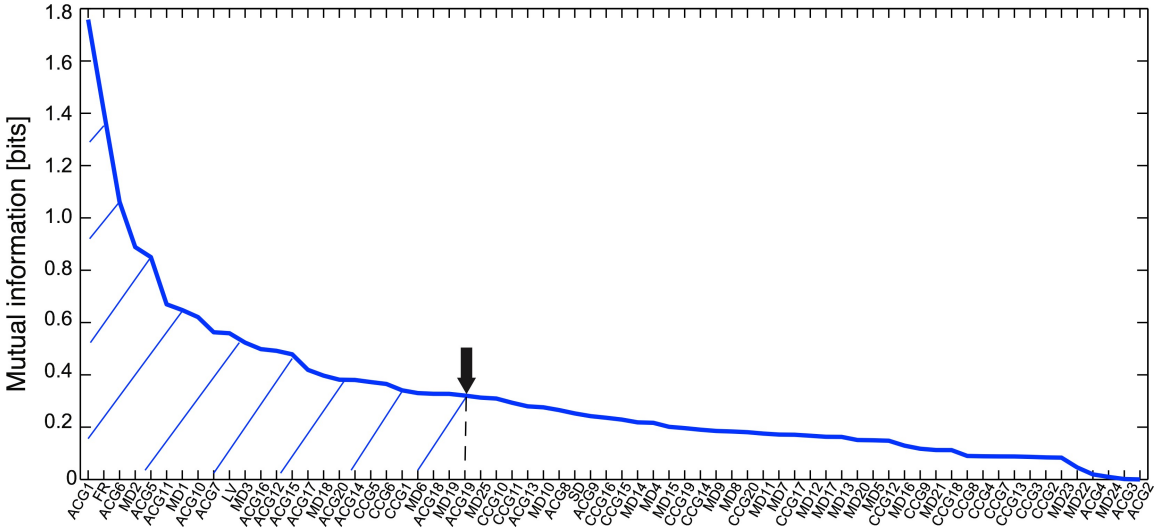

Figure 3-2: Mutual information of the sixty-eight FVs
Mutual information concerning g_i and g_c values plotted in bits for the sixty-eight FVs. Hatch and downward arrow indicates the twenty-five FVs selected for PCA.

3.3 Principal component analysis

PCA was conducted for a total of 1100 spike segments (ten segments each for the 110 IO neurons), containing 440 segments for 44 neurons sampled in five PIX experiments, 110 segments for 11 IO neurons sampled in two CBX experiments and 550 segments for

FV	Rank	MI	Sensitivity		FV	Rank	MI	Sensitivity	
			g_i	g_c				g_i	g_c
ACG1	1	1.76	+++	n	ACG15	14	0.48	+	+
FR	2	1.41	+++	n	ACG17	15	0.42	+	+
ACG6	3	1.06	++	+	MD18	16	0.40	+	+
MD2	4	0.89	++	+	ACG20	17	0.38	+	+
ACG5	5	0.85	++	n	ACG14	18	0.38	+	+
ACG11	6	0.67	+	+	CCG5	19	0.37	+	+
MD1	7	0.65	+	+	CCG6	20	0.36	+	+
ACG10	8	0.62	++	+	CCG1	21	0.34	+	+
ACG7	9	0.56	+	+	MD6	22	0.33	++	+
LV	10	0.56	+++	+	ACG18	23	0.33	+	+
MD3	11	0.52	+	+	MD19	24	0.33	+	+
ACG16	12	0.50	+	+	ACG19	25	0.32	+	+
ACG12	13	0.49	+	+					

Table 3.1: Sensitivity of top ranked twenty-five FVs to changes of g_i and g_c
List of top twenty-five FVs ranked by mutual information (MI) and its sensitivity to the changes of g_i and g_c which indicated by n/+/++/+++ for non/low/medium/high sensitivity, respectively.

55 IO neurons sampled in seven CON experiments. Then, the FVs of SIM data were projected into the PCA space for construction of the forward model. We selected top three PCA axes for the following two reasons. First, eigenvalues were high for the first two axes (0.27 and 0.21, respectively) and sharply decreased for the third one (0.09), with the sum of eigenvalues for the top three axes amounting up to 0.57. Second, MI was accordingly high for the first two axes (1.6 and 1.1 bits, respectively), significantly reduced for the next axis (0.63) and remained rather low for the remaining axes. These findings indicate that the top three PCA axes conveyed reliable information on the g_i and g_c estimation.

Figure 3-3 indicated that the first two PC components of SIM data mainly conveyed information of g_i, whereas the third component conveyed information of both g_i and g_c. This result suggested that the estimated distribution might differ between g_i and g_c. The estimated g_i distribution should be sharper than that of g_c because of the good distinguishability of the g_i variable.

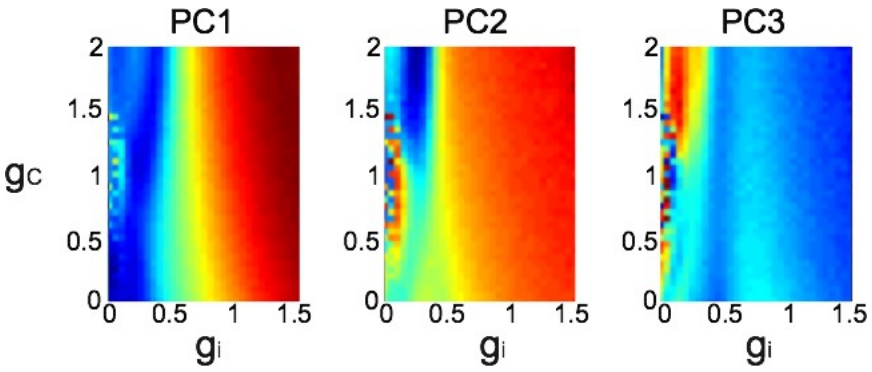

Figure 3-3: Maps of top three PC components for g_i and g_c
3-dimensional maps of the three PCA components plotting the mean of PC scores for g_i and g_c by pseudo-color representation. The color-map is normalized by the peak values.

We also studied the effects of number of FVs for three-dimensional PCA space as the evidence for Bayesian estimation (8.06×10^{-5} for fifteen FVs, 1.05×10^{-4} for twenty-five FVs, and 4.88×10^{-5} for thirty-five FVs), and selected the twenty-five FVs that exhibited the highest evidence value. They included ACG1, FR, etc., rejecting ACG2, ACG3, SD, etc. (MI and rating, 0.0001 and 68^{th}, 0.0017 and 67^{th}, and 0.25 and 32^{nd}, respectively). Those FVs were found to convey more than 70% (hatched area in Figure 3-2) of the g_i and g_c information (down ward arrow in Figure 3-2).

3.4 Coverage of the SIM data over the EXP data

Finally, we confirm that simulation data can faithfully reproduce the firing dynamics of experimental data, as shown in the feature space. Bayesian inference requires for the forward model of SIM data to completely cover the distribution of EXP data, which was guaranteed by expanding g_i and g_c ranges for SIM data much wide than those supposed for EXP. Figures 3-4A-C show that this requirement is satisfied by mapping SIM (blue symbols) and EXP spike data for PIX, CBX, and CON (red, green and black symbols) into the 3-dimensional PCA space. We confirmed that SIM spike data completely cover the distributions of EXP spike data except for a fraction of PIX data of one animal (red diamonds). Wide distribution of PCA scores for SIM

data is not due to large variances but because of wider ranges of g_i ([0–1.5 mS/cm^2]) and g_c ([0–2.0 mS/cm^2]) for SIM data than those for EXP (SIM and EXP: 3±5.5 and 0±2.6 for PC1, -1.9±3.3 and 0±2.3 for PC2, and -1.2±1.9 and 0±1.4 for PC3).

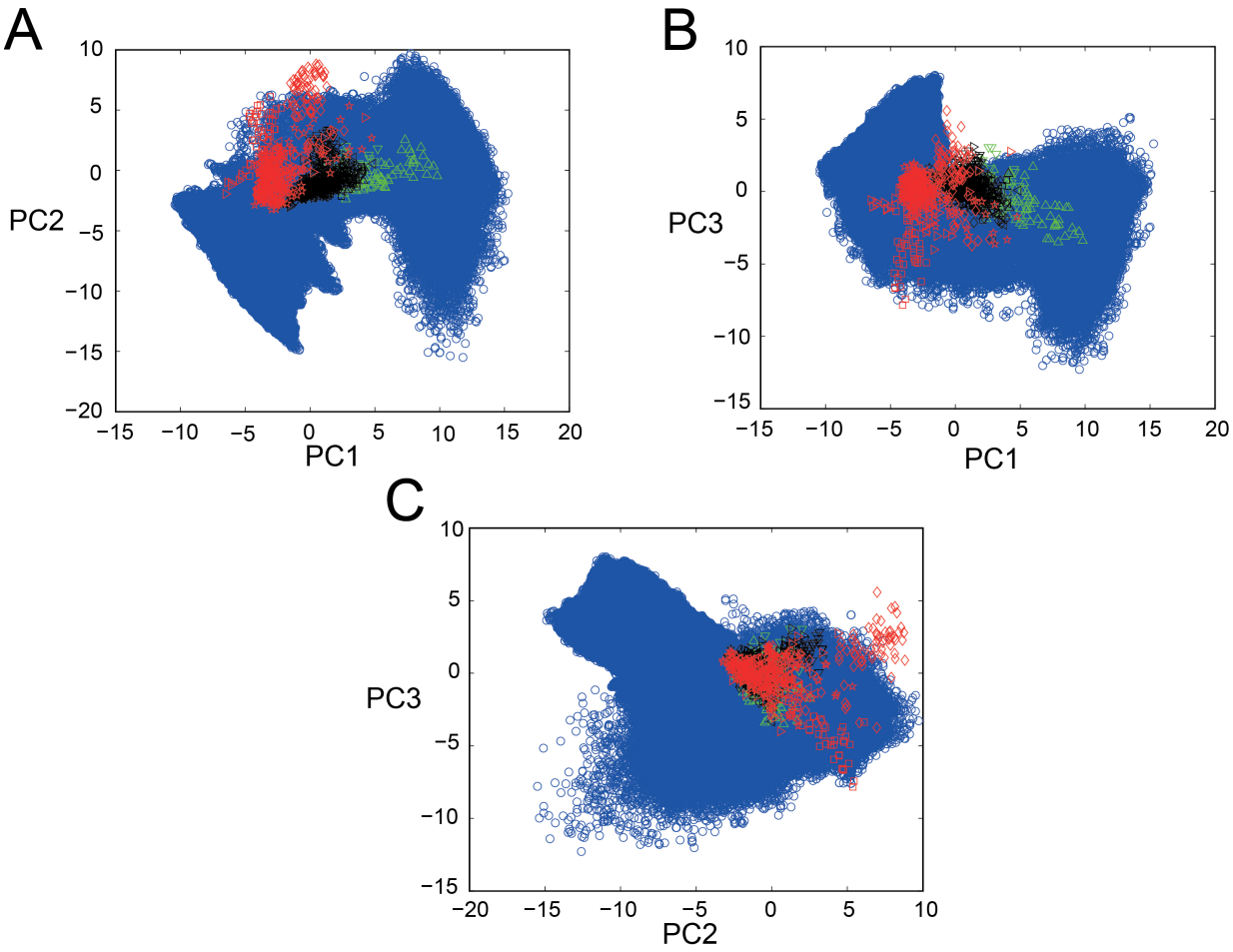

Figure 3-4: Scatter plots of EXP and SIM spike data in the 3-dimensional PCA space A-C: 2-dimensional projection views (PC1-PC2; PC1-PC3; PC2-PC3) of the scatter plots for 440, 550, and 110 spike segments for five, seven, and two animals for the PIX (red), CON (black), CBX (green) conditions, and over fifteen-million spike segments for SIM spike data (blue symbols) for 1,271 combinations of g_i ([0–1.5 mS/cm^2]) and g_c ([0–2.0 mS/cm^2]).

3.5 Discussions

In feature-based estimation techniques, selecting the features is a very difficult task because of the three following problems. The first problem is to evaluate the complicated dynamics of the EXP data to be able to estimate the goodness of the fit between the SIM and EXP data. This was resolved by using sixty-eight features to capture various aspects of neuronal activity. One-third of the FV components characterize temporal properties, while the rest of the components quantify spatial properties of the firing patterns. Second, the feature set should be informative on the model parameters to be estimated. Otherwise, it induces the estimation noise, and thus impairs the accuracy of the estimation. We resolve this problem by computing the mutual information of the g_i and g_c conveyed by each feature. This step has been shown very effective in retaining rich-information features and eliminating the poor ones. For instance, the spike distance (SD) [35], which expresses the synchrony of firing across neurons, seems to be a good candidate. However, we evaluated the SD for simulation data and found that mutual information of SD is 0.25 bits, which is significantly smaller than those for MDs (0.9 bits) and CCGs (0.4 bits). Sensitivity profiles of the SD to g_i and g_c were also similar to those of MDs and CCGs. The SD was ranked at 32^{nd}, which is far below the selection criteria for the FVs (only top twenty-five were selected), we thus ignored the SD in the feature vector. Third, since all features are derived from a spike pattern, they are highly correlated in such a way that it would be duplicate information found in another ones. We conducted the principal component analysis to reduce the redundancy in those features, and finally selected the top three principal components for constructing the forward models. As a consequence, we can extract compact but still informative feature vectors from the spike train data.

There was an additional improvement in construction of the simulation model compared to our previous study [49], which is the length of the simulation spike data was significantly extended from 500s to 5,000s. There are two reasons for the extension. First, we found that the length used for the simulation data in the pre-

vious study (500s) was insufficient to cover the spatiotemporal dynamics of the IO spike data, and thus generated 10× longer (e.g, 5,000s) simulation data to ensure more satisfactory reproduction of the IO firing dynamics (cf. Figure 3-4). Second, the Bayesian method requires a quite large training data set to infer reliable estimates. Therefore, a total of over fifteen million spike data was generated to construct the forward model. Altogether, we confirm that the experimental data was reliably reproduced despite the imperfectness of the model.

Chapter 4

Results: Validation of the proposed approaches by simulation data

The inverse problem of estimating model parameters from spike trains needs a stochastic approach to find most likely solutions among many possible ones. Since the brain exhibits complicated dynamics that is difficult for the model to reproduce, the modeling errors are inevitable. In Chapter 2, we proposed two different approaches: the Bayesian inference and the minimum-error method. These stochastic approaches are supposed to reduce the mismatch between the model and the brain, and thus improve the estimation precision. However, nature of the inverse problem makes it impossible to verify estimation performance in theirs application to experimental data. Validation of the previously developed methods is thus desired. Adopting the same task of estimating two conductance values in the IO network model, in this chapter, we utilize simulated spike data as the test data. Unlike the experimental data, the underlying conductance values are known for the simulation data, which are thus suitable for validation purpose. We confirmed that both the minimum error and the Bayesian methods are suitable for resolving the inverse problem despite the imperfectness of the model, but the segmental Bayes is strongly recommended for highly non-stationary spike data.

4.1 Validation of the minimum-error method

In the previous study [49], we developed the minimum-error method to estimate the two parameters from IO spike data. We found that the simulated neurons did not perfectly reproduce the firing dynamics, and thus divided the experimental spike data into short time segments and estimated two model parameters for each time segment by minimizing the distance between the simulated and experimental spike data. Then, the distribution of the estimated parameter values from all segments was treated as a population of estimates. This simple algorithm worked fairly well, as indicated by the extremely small errors between the experimental and simulation spike data in the feature space. Here, we perform a simple validation of the minimum-error method using simulation data. Three representative conductance values that display qualitatively different firing dynamics were selected to generate the test data. The results for the test data demonstrated that the minimum-error method is effective for resolving the inverse problem [17].

4.1.1 Test data sets

For three representative model parameter sets of (g_i,g_c) = (0.4,1.4) (♯1), (1.4,1.4) (♯2), and (1.4,0.4) (♯3), we simulated the test spike data for validation. The three parameter sets were selected for the following two reasons. First, they exhibited firing dynamics significantly different from each other. Second, they imitate the three types of experimental conditions, *i.e.*, administration of GABA blocker picrotoxin (PIX) and gap-junction blocker carbenoxolone (CBX) and their control (CON), in our previous study [49]. We applied the minimum-error method to estimate g_i and g_c from the test spike data and evaluated the estimation accuracy as the absolute error between the estimated and true parameter values.

4.1.2 Quantitative analysis of test data

Raster plots are drawn in Figure 4-1 for spike trains in 50 s for three representative neurons in the test data. While neurons under condition ♯1 constantly fired at a very

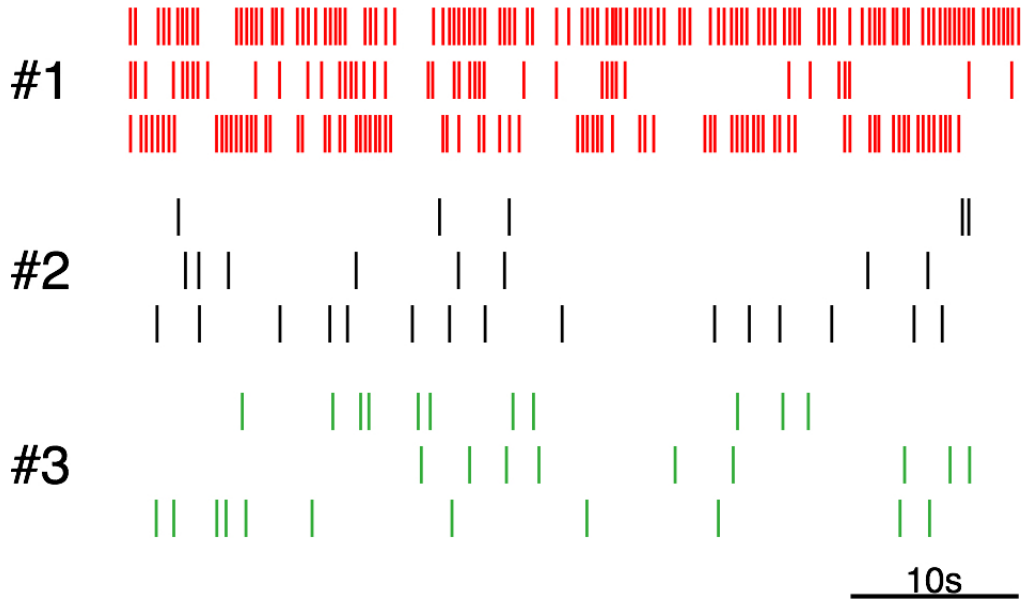

Figure 4-1: Spike trains of the test data sets
Raster plots in 50s of three representative neurons in the test data sets (♯1, red traces, ♯2, black traces, and ♯3, green traces)

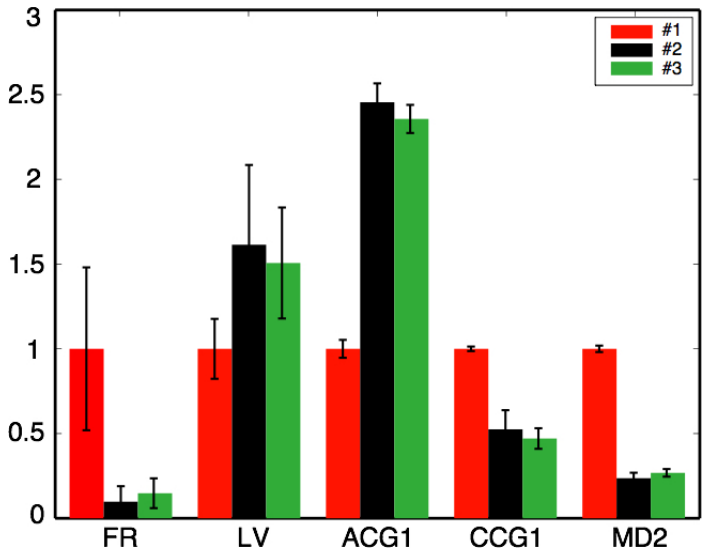

Figure 4-2: Five major features of test spike data
Five major features (FR, LV, ACG1, CCG1, and MD2) extracted from spike data of 9 neurons in the three condition. Each feature was normalized by the averaged value of the ♯1 data

high frequency (> 1.5 Hz), the firing rates of neurons in the other two data sets were rather low (< 0.2 Hz). This should be because increasing the inhibitory synaptic strength g_i makes the neurons fire less frequently.

Next, we analyzed the firing dynamics of the test data in terms of the five major features averaged over nine neurons under the three conditions (♯1, ♯2, ♯3) (Figure 4-2). For three features (FR, CCG1, and MD2), condition ♯1 showed significantly higher values than for other conditions, whereas the situation was opposite for the other two features (LV and ACG1). These changes in the features indicate that the firing dynamics became more frequent and more regular in the individual neurons and more synchronous across the neurons under condition ♯1.

4.1.3 Parameter estimation for the test data

We applied the minimum-error method for 50 s spike trains in the test data sets and separately calculated the accuracy as the absolute difference between the estimated and true parameter values of g_i and g_c. Figure 4-3 shows the mean and standard deviation of the errors in g_i and g_c estimates for the test data. Errors of g_i estimation for all three test data sets were significantly smaller than those of g_c, being approximately 8% and 35% of the parameter range, respectively.

The analysis of variance (ANOVA) indicated that there were significant differences of the g_i and g_c errors across both factors: the type of parameters (g_i or g_c) ($p = 1.43 \times 10^{-29}$) and the parameter values among test data sets ($p = 5.84 \times 10^{-11}$) (Table 4.1). These results indicate that the accuracy of the minimum-error method depends upon both the types and the values of the parameters to be estimated. It should be noted that the error is relatively large for the g_c estimates. Since g_c controls coupling among the neurons, the level of synchrony, such as CCG1, might contain useful information on the g_c value. As indicated by CCG1 in Figure 4-2, the level of synchrony does not change too much among the three data sets (♯1, ♯2, ♯3). This might be the reason why the g_c estimates were not particularly accurate.

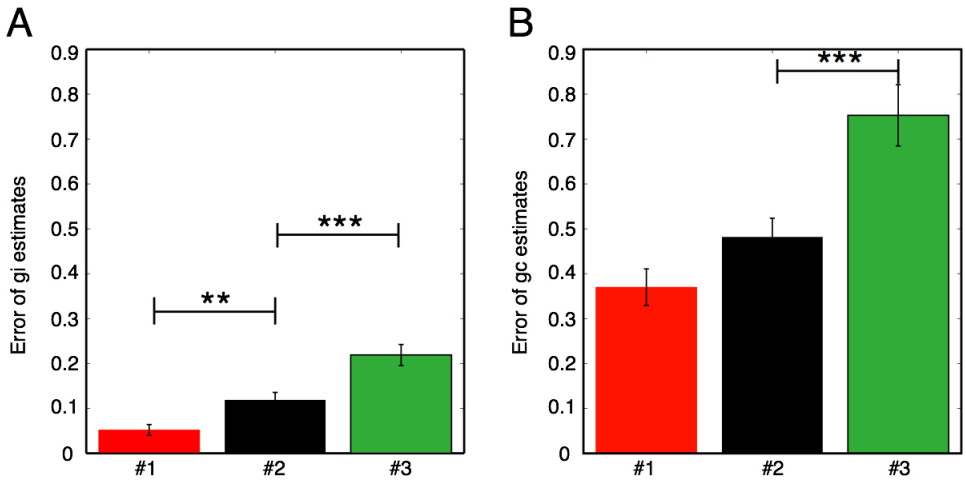

Figure 4-3: Estimation errors for nine neurons in the test data
Errors of g_i (A) and g_c (B) estimated by the minimum error method for 50s spike data of 9 neurons. Asterisks represent the significance level by t-tests across the conditions. $^{**}p < 0.001$, $^{***}p < 0.0001$.

	♯1	♯2	♯3
g_i	0.05 ± 0.01	0.12 ± 0.02	0.22 ± 0.02
g_c	0.37 ± 0.04	0.48 ± 0.04	0.75 ± 0.07
F(♯1,♯2,♯3)	25.54 ($p = 5.84 \times 10^{-11}$)		
F(g_i,g_c)	159.72 ($p = 1.43 \times 10^{-29}$)		

Table 4.1: Estimation errors of g_i and g_c for test data

4.1.4 Dependence of the estimation error on the spike data length

We further investigated the effect of the spike data length on the estimation accuracy. The parameters were estimated under different settings of the data length, which was varied from 50 s to 500 s. These data lengths were comparable to the recording time of the experimental data in our previous study [49]. Figure 4-4 indicates that increasing the spike data length enhanced the estimation accuracy for both g_i and g_c. The amount of improvement evaluated over 500 s were about 50% for g_i estimates (Figure 4-4A) and nearly 30% for g_c estimates (Figure 4-4B) compared with those evaluated over 50 s. This result confirms that the length of 500 s used for the experimental data in our studies was long enough to obtain reliable estimates.

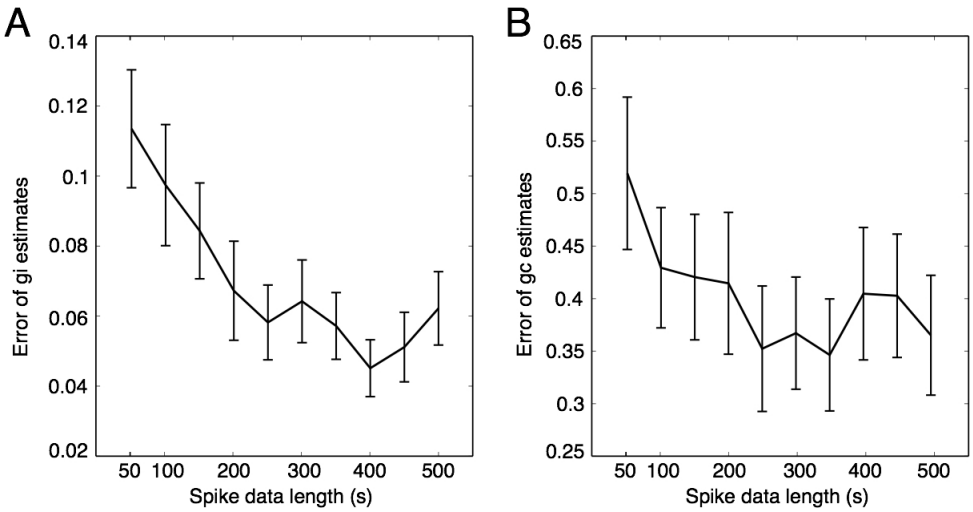

Figure 4-4: Dependence of the estimation error on spike data length
Dependence of the estimation errors of g_i (A) and g_c (B) on the spike data length which varied from 50s to 500s. Means (solid trace) and standard deviations (error bars) are of 10 trials.

4.1.5 Conclusions

In this simulation study [17], we attempted to verify the minimum-error method using simulated spike data as the test data sets. Since the true values of g_i and g_c in the test data were known, it was straightforward to evaluate the estimation errors. Two important results were obtained from our study. First, the accuracy of the minimum-error method was found to strongly depend on the firing pattern of the neurons. Synchronous pattern is important to detect changes in g_c, whereas irregular firing pattern is useful in detecting changes in g_i. Second, longer spike data can significantly improve the performance of the estimation. In conclusion, we argue that the minimum-error method is effective for resolving the ill-posedness of the inverse problem despite the imperfectness of the model.

4.2 Validation of the segmental Bayes

In Chapter 2, we proposed a stochastic approach to reduce the modeling errors by allowing the parameter values to be varied in time segments. In this segment-wise

approach, the parameters were firstly estimated segment by segment. This relaxes the condition of the parameter search and thus enables to capture the complicated firing dynamics of experimental spike data. The segmental estimates were then integrated by a hierarchical Bayesian framework, resulting in a single estimate. As a consequence, the segmental Bayes has been shown to minimize the fitting error between experimental and simulation data in the feature space.

In this section, we aim to confirm the superiority of the segmental Bayes using simulation data as the test data. The verification results indicated that the segmental Bayesian inference minimized estimation errors than the conventional Bayesian inference or the minimum error method. Robustness of the segmental Bayesian approach against highly non-stationary dynamics of the spike data was also confirmed. It thus provides an effective approach to resolve the inverse problem even when the model is an imperfect representation of the experimental data.

4.2.1 Manipulate non-stationarity for the test data

The basic idea of the segmental Bayes is to deal with non-stationary dynamics of the experimental spike data. Such non-stationarity arises typically from high-dimensional spatio-temporal system. Unfortunately, our mathematical model was not complicated enough to produce such non-stationary dynamics. Figure 4-5 shows the firing rate extracted from spike trains of representative 13 CON and 9 SIM neurons. While exhibiting a comparable mean firing frequency (around 1Hz), the SIM neurons tend to fire periodic and stable in time, as well as there is not much different in firings among those neurons (standard deviation of the firing frequency across time and neurons, 0.23 and 0.30, respectively). By contrast, firing frequency of EXP neurons vary strongly in both time and space (0.28 and 0.68). This result confirms that the simulation failed to precisely reproduce the non-stationarity of EXP data, and thus was not suitable for verifying the segmental Bayes.

To overcome the aforementioned issue, we manipulate the test data so that it imitates the firing dynamics of EXP spike data as follows. Suppose that the test spike data was selected at a parameter value $g = (g_i, g_c)$, from which we generate

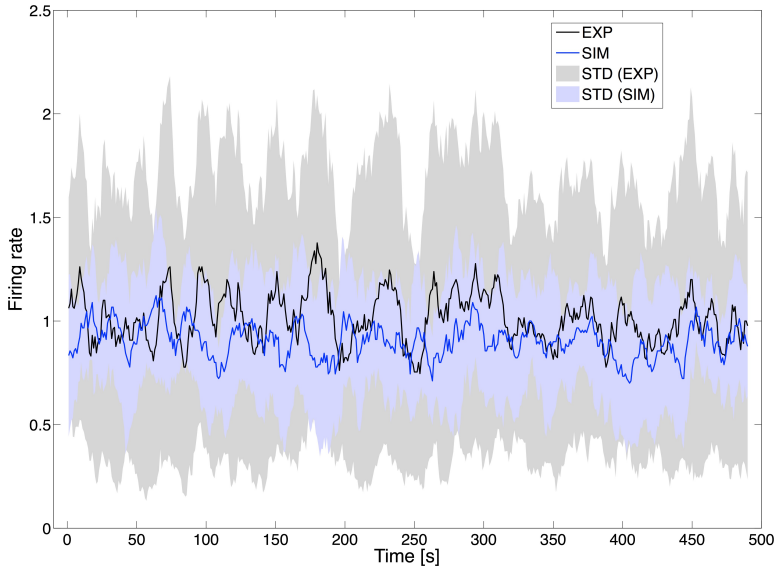

Figure 4-5: Firing rate of experimental and simulation neurons
Firing rate averaged over 13 CON (black trace) and 9 SIM (blue trace) neurons. Shaded area represents standard deviation across those neurons.

500s spike trains. Unlike the simulation of the forward model in which the parameter value was fixed, the value of g in the simulation of test data was adjusted in every 50s. The adjusting values of g were randomly chosen from the normal (*Gaussian*) distribution $N(g, \sigma^2)$ with the mean g and the variance σ^2. Here, σ can be regarded as a parameter to control the level of non-stationarity in the test data. Then, the PCA scores $\boldsymbol{y}$ of the test data is evaluated as mentioned previously (cf. Methodology 2.2.1). We conventionally define the standard deviation of the first PCA score of $\boldsymbol{y}$ as the non-stationary level. It is worth noting that simulating non-stationarity in the test data is independent to the construction of the forward model.

It is very important to investigate the dependence of non-stationary level of the test data on the parameter σ. Figure 4-6 indicates that increasing the variance parameter σ monotonically enhanced the non-stationarity of the test data. The amount of improvement evaluated with $\sigma = 0.3$ (2.77 ± 0.8) and $\sigma = 0.5$ (3.31 ± 1.01) were about 113% and 155%, respectively, compared to that evaluated with $\sigma = 0.1$ (1.3 ± 0.38). The result specifies that the test data was reliable to elicit advances of the segmental Bayes in estimating parameter for high non-stationary spike data.

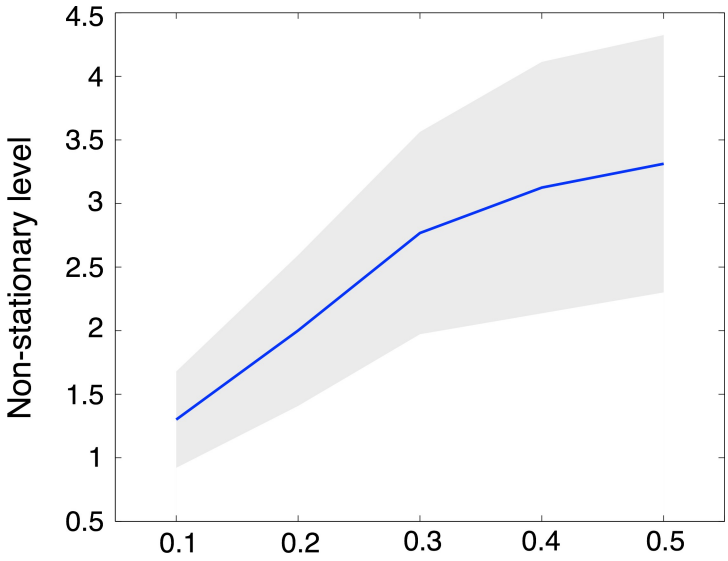

Figure 4-6: Dependence of non-stationary level on the parameter σ
Solid and shaded area, mean and standard deviation over 100 trials at each σ in the range of ([0.1–0.5]).

4.2.2 The estimation error for the test data

For each test data, we applied three different approaches to estimate the parameter values (g_i and g_c). They are the segmental Bayes, the non-segmental Bayes and minimum error method. The test data sets were generated by a random set of 100 parameter values $g = (g_i, g_c)$ for varied parameter σ in the range [0.1–0.5].

Figure 4-7 shows the absolute differences between the estimated and true parameter values of g_i (Figure 4-7A) and g_c (Figure 4-7B), independently. Segmental Bayes outperformed both non-segmental Bayes and minimum error method for g_i and g_c estimation for all non-stationarity levels. These results are consistent with our view that the segmental Bayes minimizes errors in g_i and g_c estimates because of the non-stationary firing dynamics. For the two comparative approaches, there was a tendency that increasing the non-stationary level of the test data decreased the accuracy of both g_i and g_c estimation, whereas it was not so for the segmental Bayes (Figure 4-7B). This finding indicates that segmental Bayes is strongly robust against the non-stationarity of the spike data.

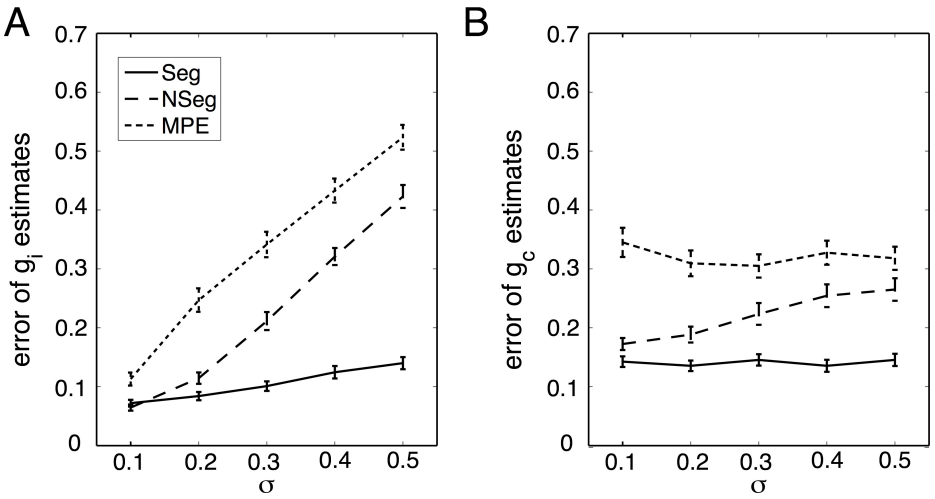

Figure 4-7: Estimation errors by three approaches
Estimation errors of g_i (A) and g_c (B) using the segmental Bayes (Seg, solid trace), the non-segmental Bayes (NSeg, dashed trace) and minimum error method (MPE, dotted trace). Error bars are standard deviations across 100 trials.

4.2.3 Robustness of the segmental Bayes

Finally, we tested the superiority of the segmental Bayesian inference over the two comparative approaches in terms of the combined estimation error (Euclidean distance between the true and estimated values in the (g_i, g_c) space). The magnitude of the estimation error was smaller for the segmental Bayesian inference (Figure 4-8) than that for non-segmental Bayes and minimum error method across the three non-stationary levels. The statistical significance of the estimation errors was largest ($p = 4.6 \times 10^{-10}$ and $p = 2.3 \times 10^{-24}$ by t-tests between Seg-NSeg and Seg-MPE, respectively), moderate ($p = 6.9 \times 10^{-5}$ and $p = 1.3 \times 10^{-23}$) and minimum ($p = 0.5$ and $p = 1.1 \times 10^{-14}$) for $\sigma = 0.5$, $\sigma = 0.3$ and $\sigma = 0.1$ values, respectively, corresponding to the level of the non-stationarity of the test data sets. These findings confirm that segmental Bayesian inference performs much better than the other methods in cases of highly non-stationary spike data.

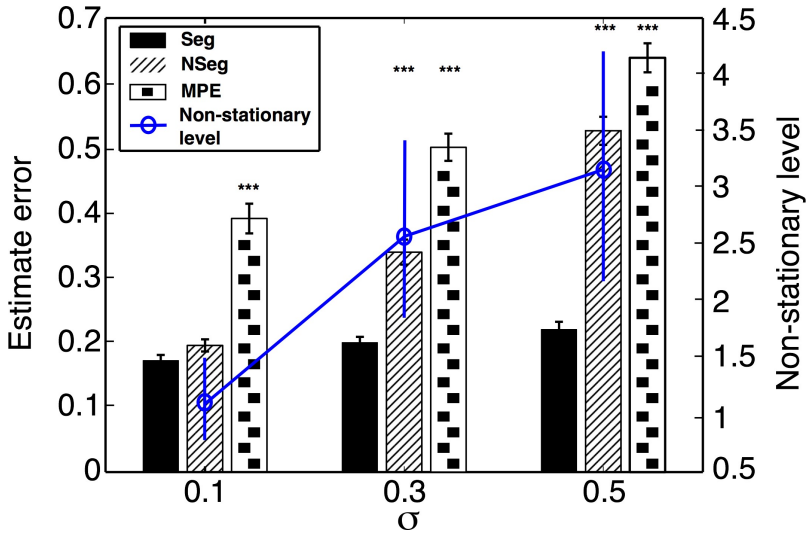

Figure 4-8: Robustness of the segmental Bayesian inference to the non-stationarity Superiority of segmental Bayesian method (Seg, solid columns) over two other methods (NSeg, hashed columns and MPE, dotted columns) at three non-stationary levels of test data sets. The non-stationary level of the test data (blue trace) is from the results of Figure 4-6. Asterisks represent the significance level by t-tests between Seg-NSeg and Seg-MPE. $***p < 0.0001$.

4.2.4 Conclusions

We attempted to verify the segmental Bayes approach using simulated spike data as the test data sets. Due to a rather low complexity of the model, the simulation data used for constructing the forward model is not suitable for the verification purpose. We thus manipulated the non-stationarity in the test data by adjusting the parameter values during the simulation. Since the true values of g_i and g_c were known in the test data, it was straightforward to evaluate the estimation errors. The two important findings in our previous study were confirmed from this study. First, segmental Bayes significantly reduced the estimation errors compared to the two comparative methods. Second, it was robust to the non-stationarity of the spike data. These results suggest that segmental Bayes is highly recommended for estimating the model parameters from spike data of real neurons that usually exhibits highly non-stationary dynamics. In conclusion, we argue that the segmental Bayesian inference is a useful tool to resolve the inverse problem even in the presence of the imperfectness of the model.

Chapter 5

Results: Parameter estimation for experimental spike data

The present study aims to estimate the conductance of the inferior olive (IO) neurons from spike train data using the network model simulation, which is confronted by various mismatch problems in the system complexity between the model and experimental data. The first is the granularity-hierarchy mismatch. The experimental spike data are generated by the network while the parameters to be estimated exist at the synapses. The second is the degrees of freedom mismatch. The real IO conveys far more complicated structures with huge degrees of freedom than those for the model, the number of IO neurons being at least four orders of magnitude greater than that for the model. The third mismatch is that IO firing dynamics are highly non-stationary, showing chaos, oscillations and other non-stationary properties [58], while those of the model convey rather low non-stationarity. Therefore, we cannot expect that the network model can perfectly simulate the experimental data.

In Chapter 2, we introduced a novel methodology to resolve the inverse problem in the presence of the imperfectness of the model. Given the experimental spike train in three different conditions, we extracted twenty-five features selected from the mutual information calculation, conducted PCA to reduce the redundancy among those features, and then selected top three PC components for the estimation purpose. In this chapter, we show the estimations for the experimental data using three differ-

ent methods: the segmental Bayes, the non-segmental Bayes which conventionally estimates g_i and g_c for the entire spike data, and the minimum error method, which determines the estimates as the closest match in the PCA space. Because of the nature of the inverse problems, in which the true parameter values are unknown, we evaluated the performance of these methods by the distance in the PCA space between the experimental data and the simulation data generated by the corresponding estimated parameters. The segmental Bayes was found to outperform the two comparative methods by minimizing the PCA error. The non-stationarity is coherently in agreement with the performance of the three methods, being high, medium and modest for the segmental Bayes, the non-segmental Bayes, and the minimum error method, respectively. We argue that segmental Bayes is an effective tool to estimate the model parameters from spike data of real neurons which typically exhibit complicated firing dynamics.

5.1 Experimental data

It is important to note that the Purkinje cell's complex spikes bear a one-to-one relationship to IO neuronal spikes, and thus can be used as proxies for IO spike trains. We used the spike data collected from two picrotoxin (PIX; [37, 36]) and one carbenoxolone (CBX; [9]) studies. These studies sampled the IO spike as the complex spikes of Purkinje cells and blocked the inhibitory and gap-junctional conductance (g_i and g_c) of IO neuronal circuitry by application of PIX and CBX. PIX and CBX experiments contained the spike data of 500-second-long samples from 136 and 35 neurons, respectively (Table 5.1).

Figures 5-1 shows the CS spike trains of nine representative PCs (1–9) in the CBX, CON and PIX conditions. The firing frequency of CS activity became much more frequent (50% increase) and oscillatory in the PIX than the CON condition and vice versa (50% decrease) in the CBX condition. Notice also that the firing dynamics significantly fluctuate: dense at certain times and sparse at others. Such non-stationary firing dynamics makes it very difficult for the model to reproduce.

Animal No.	EXP condition	Neurons	Reference
1	CBX	22	[9]
2	CBX	13	
3	PIX	16	[37, 36]
4	PIX	25	
5	PIX	42	
6	PIX	32	
7	PIX	21	

Table 5.1: Experimental spike data

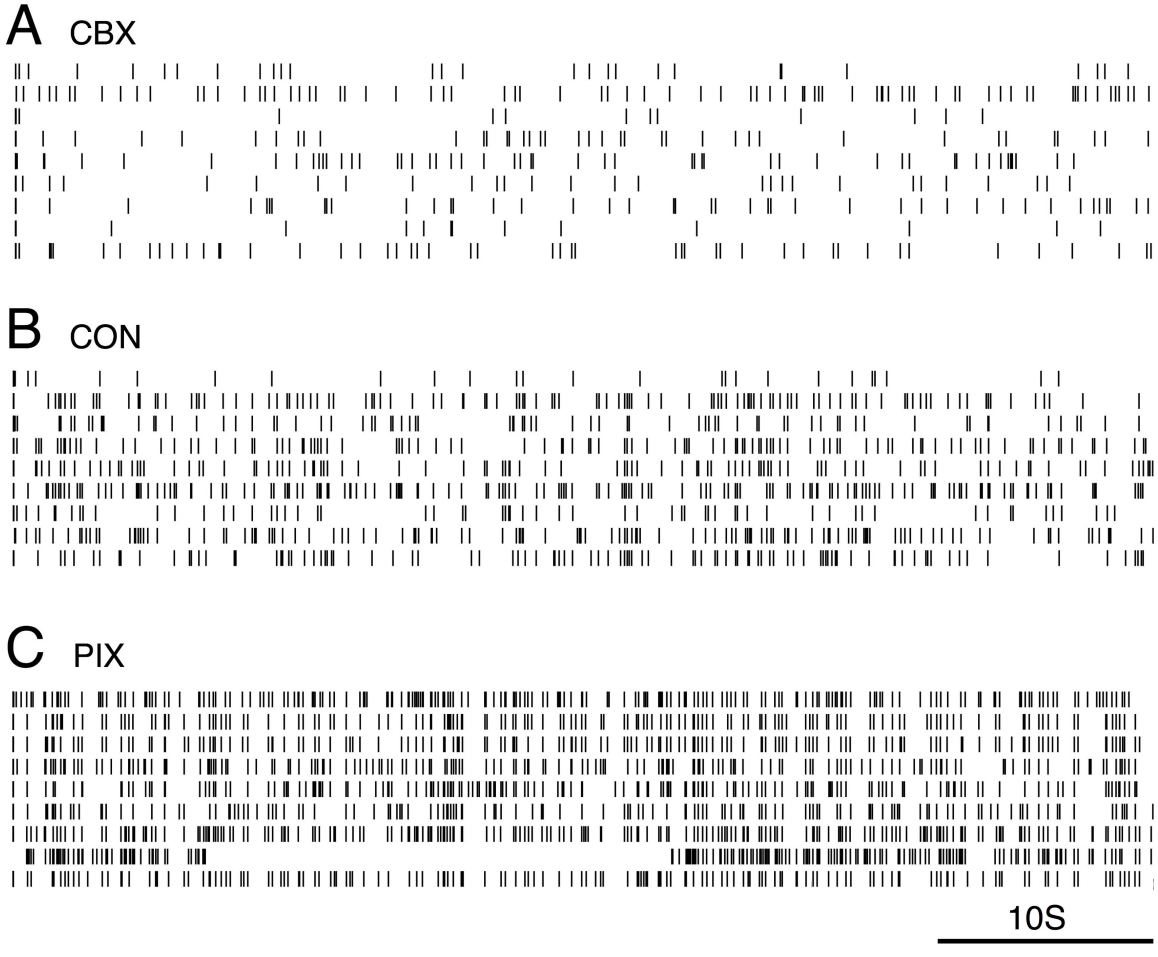

Figure 5-1: The spike trains in 50s of nine representative EXP neurons in the three conditions

5.2 Feature evaluation for experimental spike data

Next, we analyze the firing dynamics of the EXP spike data in terms of the feature vectors that were selected by calculating the mutual information between each feature and the parameter space (cf. Table 3.1). Figure 5-2A shows the five major FVs (FR, LV, ACG1, CCG1 and MD2) averaged for 660 CON (for 440 PIX and 220 CBX experiments), 220 CBX, and 440 PIX spike segments each for 55 (44 and 11 for PIX and CBX experiments), 11, and 44 IO unit ensembles, respectively. Three of the five FVs (FR, CCG1 and MD2) increased in the PIX than in the CON condition, and vice versa for the CBX condition, whereas LV and ACG1 showed the opposite change, being lower in the PIX and higher in the CBX condition. The changes in the FVs elucidate the firing dynamics, which became more frequent in the individual IO neurons and more synchronous across the IO neuronal ensemble under the PIX than the CON condition, and showed the opposite changes under the CBX condition.

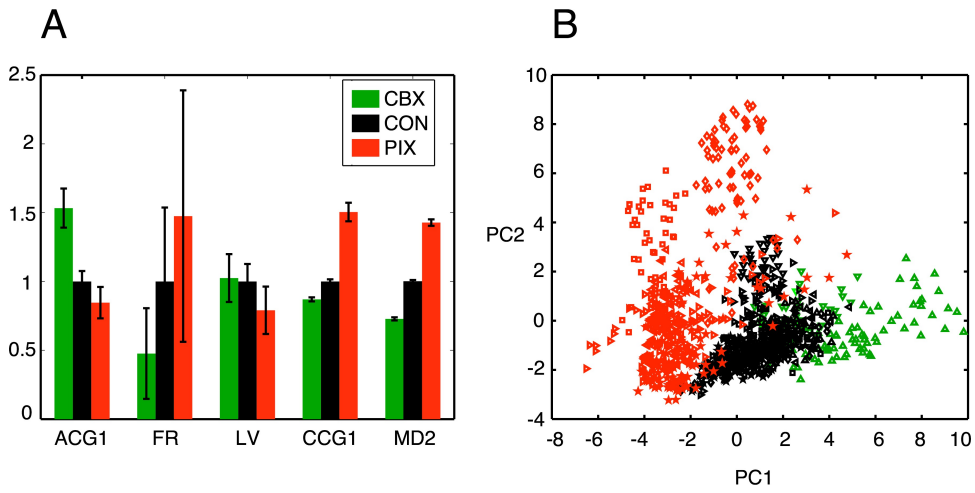

Figure 5-2: Feature evaluation of the EXP spike data
A: Five major features (FR, LV, ACG1, CCG1 and MD2) extracted from the spike data of CBX (green columns), CON (black columns) and PIX (red columns) conditions. The color conventions of EXP data are the same in the following figures. B: scatter plots of EXP data in 2D PCA.

We conducted PCA to obtain a simpler measure of the firing dynamics evaluated by the twenty-five FVs for CON, PIX, and CBX conditions. The calculation of eigenvalues indicated that the first two orthogonal components explained a major

part of the firing dynamics (first and second components, 0.27 and 0.21, respectively) and sharply decreased for the third one (0.09), with the sum of eigenvalues for the top three axes amounting up to 0.57. The EXP spike segments for the CON, PIX, and CBX conditions formed three clusters along the first PCA axis, with an overlap of the CON and CBX clusters (Figure 5-2B). The analysis of variance (ANOVA), however, indicated that there was significant difference of the top three PC components across the three conditions ($p = 2.17 \times 10^{-41}$, Table 5.2).

Condition	CBX	CON	PIX
PC1	4.41±2.21	0.93±1.27	-2.27±1.71
PC2	-0.27±0.98	-0.79±1.24	1.05±2.98
PC3	-0.4±1.46	0.28±0.88	-0.25±1.91
F(CBX-CON-PIX)	96.34 ($p = 2.17 \times 10^{-41}$)		

Table 5.2: ANOVA of the top three PC components

Figure 5-3 shows the contribution, defined as the product between the FV values and the coefficients of the FVs for the twenty-five selected FVs to the first PCA component. The major contributors to the PCA scores, such as FR, LV, and CCG1 were positive except for LV and MD2, which was negative. This finding is consistent with the locations of EXP spike segment clusters for CON (middle), PIX (leftmost), and CBX (rightmost) conditions in Figure 5-2B, and also the changes of the FVs for those conditions in Figure 5-2A.

5.3 Effect of the neuronal constraint

In this section, we demonstrate how the segmental Bayes incorporates the neuronal and commonality constraints as estimating the parameters. We found that the EXP spike data were significantly non-stationary (cf. Figures 5-7B-D), which may cause errors in the Bayesian estimation of g_i and g_c. Those errors were minimized by the segmental Bayes whereby the entire spike data for each IO neuron was fractionated into ten segments. Bayesian estimation of g_i and g_c was conducted segment by segment, under the commonality constraint that the g_i estimates agree between CBX

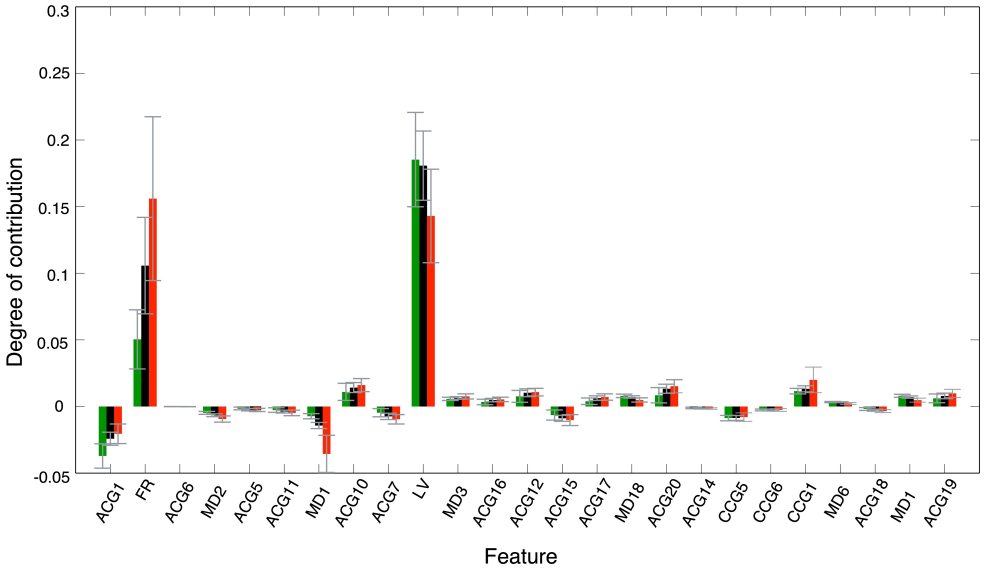

Figure 5-3: Contribution of the twenty-five features to the first PCA component
Contributions of selected twenty-five feature vectors to the first PCA axis. The mean and SD were computed for all PIX, CON, and CBX spike segments.

and CON, and the g_c estimates between PIX and CON, respectively, and the segmental estimates were finally merged into a single estimate for every neuron under the neuronal constraint assuming a single g_i and g_c for each neuron.

Figures 5-4A-D are pseudo-color representation of the posterior probability of g_i and g_c estimated for a representative IO neuron by the Bayesian inference under the commonality and the relaxed neuronal constraint ($\sigma = 10$, cf. Equation 2.15). The estimates were diffused broadly for all of the three conditions probably because of the fluctuations of the segmental estimates. The probability of the g_i and g_c estimate for the IO neuron for the three experimental conditions showed broad and overlapping distributions (Figures 5-4E and F).

By contrast, the g_i and g_c of the same IO neuron as in Figure 5-4 estimated by Bayesian inference under the optimized neuronal constraint (σ was optimized in the range of [0.1–0.5]) were sharper, with the peak of (g_i, g_c) at (0.75, 0.75 mS/cm^2) for CBX, at (0.1, 1.3 mS/cm^2) for PIX and at (0.75, 1.25 mS/cm^2) and (0.6, 1.3 mS/cm^2) for CON-CBX and CON-PIX, respectively (Figures 5-5A-F).

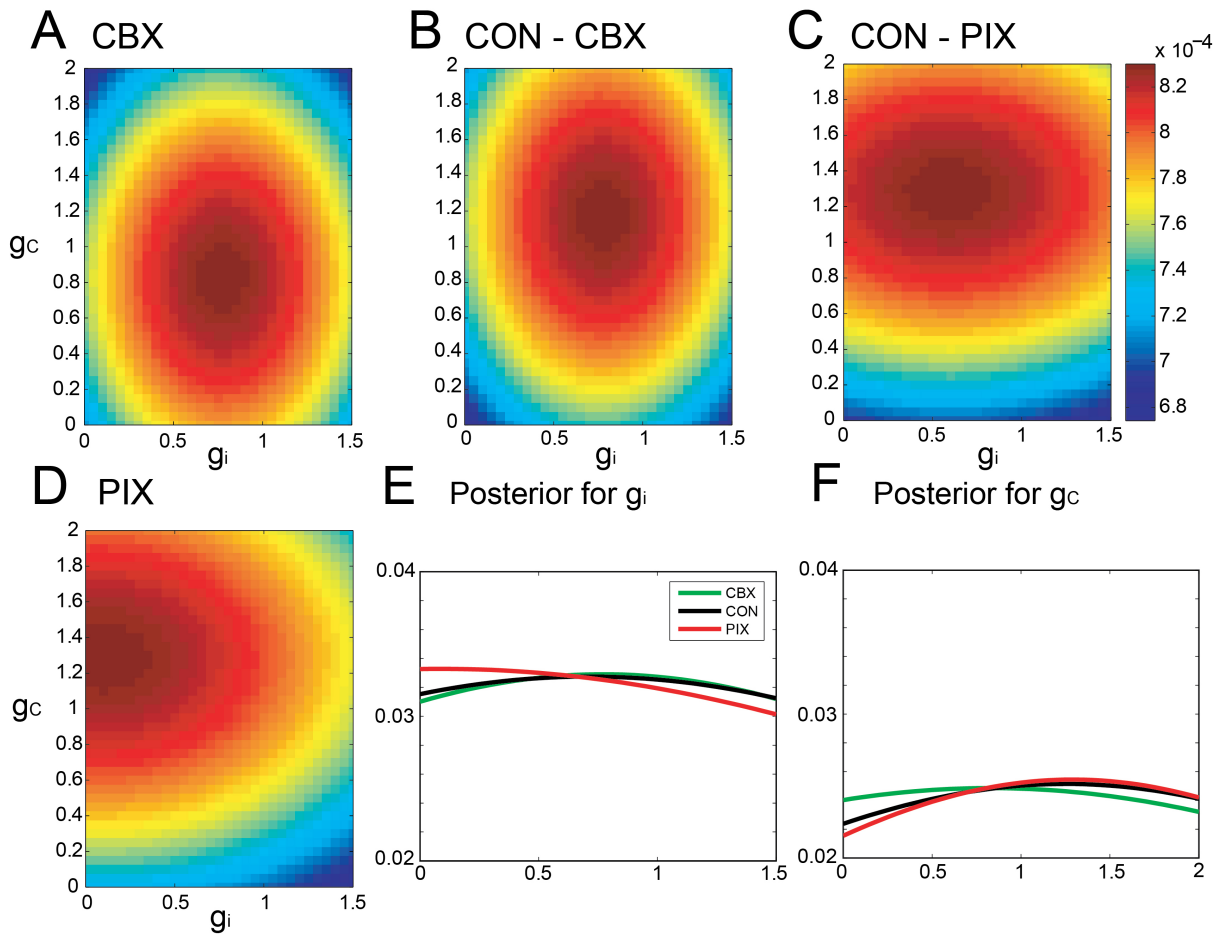

Figure 5-4: Segmental Bayesian estimates of g_i and g_c with relaxed commonality constraints

A-D, posterior probability of the g_i and g_c estimate for representative IO neurons under the relaxed commonality constraint ($\sigma = 10$, Equation 2.16) for the two experimental (CBX and PIX) and two corresponding control conditions (CON-CBX and CON-PIX). E and F, the profiles of g_i and g_c probability of the neurons plotted in A-D.

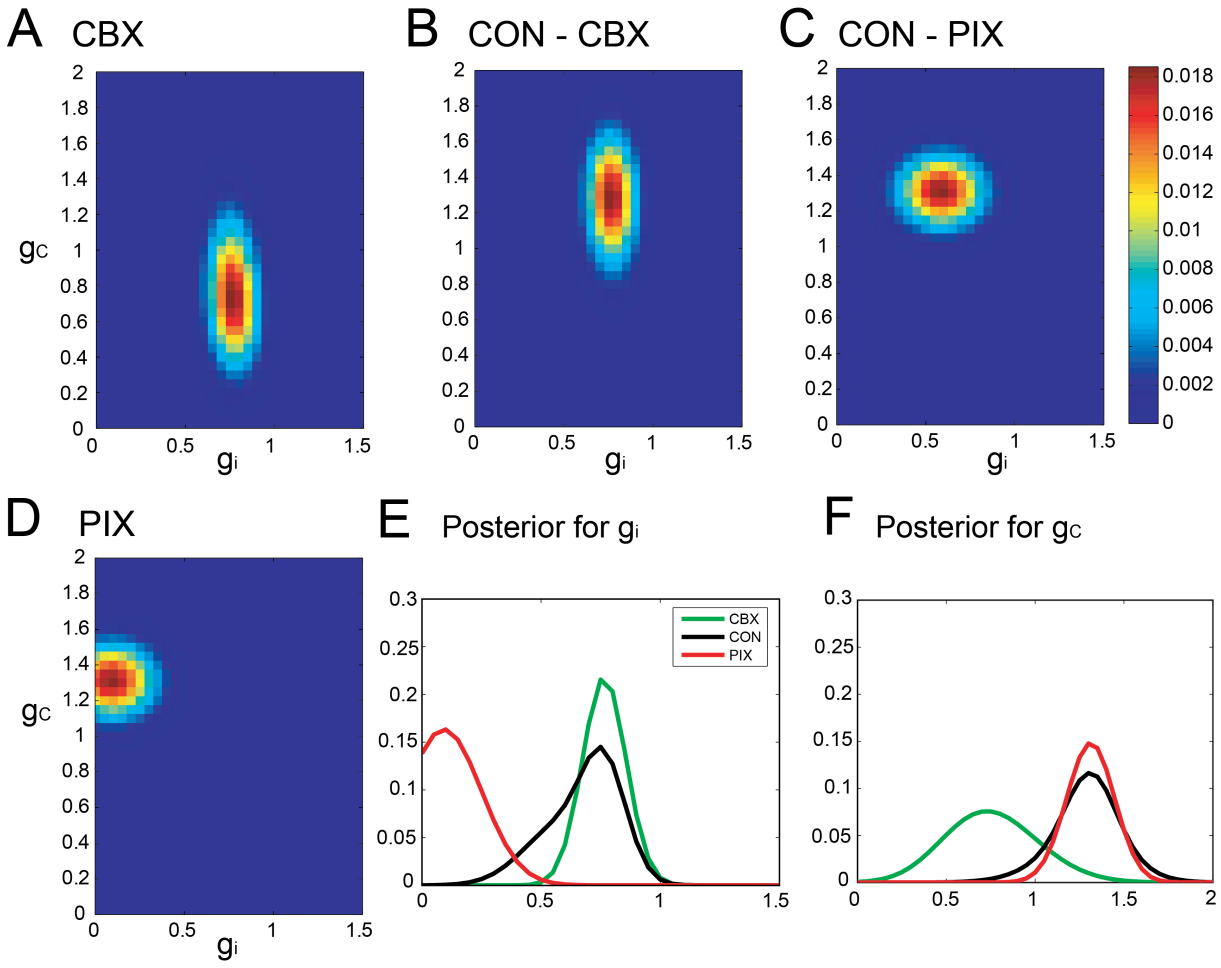

Figure 5-5: Segmental Bayesian estimates of g_i and g_c with optimized commonality constraints
A-D and E-F, similar posterior probability plots of g_i and g_c to those in Figure 5-4 but with the optimized commonality constraints.

5.4 Estimations by segmental, non-segmental Bayes and the minimum error method

Next, we compare the estimations of the EXP data by the segmental, non-segmental Bayes and the minimum error methods. Figures 5-6A and B show the ensemble distributions of g_i and g_c estimated by the segmental Bayesian inference for the entire population of IO neurons in comparison with those by the non-segmental Bayes whereby g_i and g_c were estimated at once across the entire length of spike data (Figures 5-6C and D) and the minimum error method (Figures 5-6E and F). The g_i and g_c estimates by the segmental Bayes essentially agreed with those by the non-segmental Bayes with the tendency for the segmental Bayesian inference to give a sharper distribution than the non-segmental Bayes. The g_i value peaked at 0.6–0.7 mS/cm^2 for CBX and CON and at 0.1–0.2 mS/cm^2 for PIX (Figures 5-6A and C) and the g_c for PIX and CON was 1.3 mS/cm^2. The g_c value for CBX was distributed diffusely across a wide range. We noted that the segmental Bayes gave rather conflicting estimates of g_c between the two animals. In one animal there was a marked leftward shift of the peak between the CBX and CON conditions (with a reduction of g_c, filled area in Figure 5-6B) and conversely a significant rightward shift in other animal (open area). The non-segmental Bayesian inference also showed the same results, although the difference was less clear. The same tendency also found in estimations using the minimum error method (Figures 5-6F). The reason for this discrepancy between the two animals is unclear. CBX is a nonspecific blocker of the gap-junctional conductance and may act on other ionic conductances than the gap-junction, affecting the g_c estimates. The IO units were sampled across many micro-zones of the cerebellum on which the gap-junctional conductance was dependent, being high and low in the same and different micro-zones, respectively. This heterogeneity in the g_c population may also be the cause of the discrepancy.

The estimates of g_i and g_c by the segmental Bayesian inference are in partial agreement with those of the minimum error method. Those points of agreement were the g_i for CON (0.54±0.18, 0.55±0.11 mS/cm^2 for the segmental Bayes and

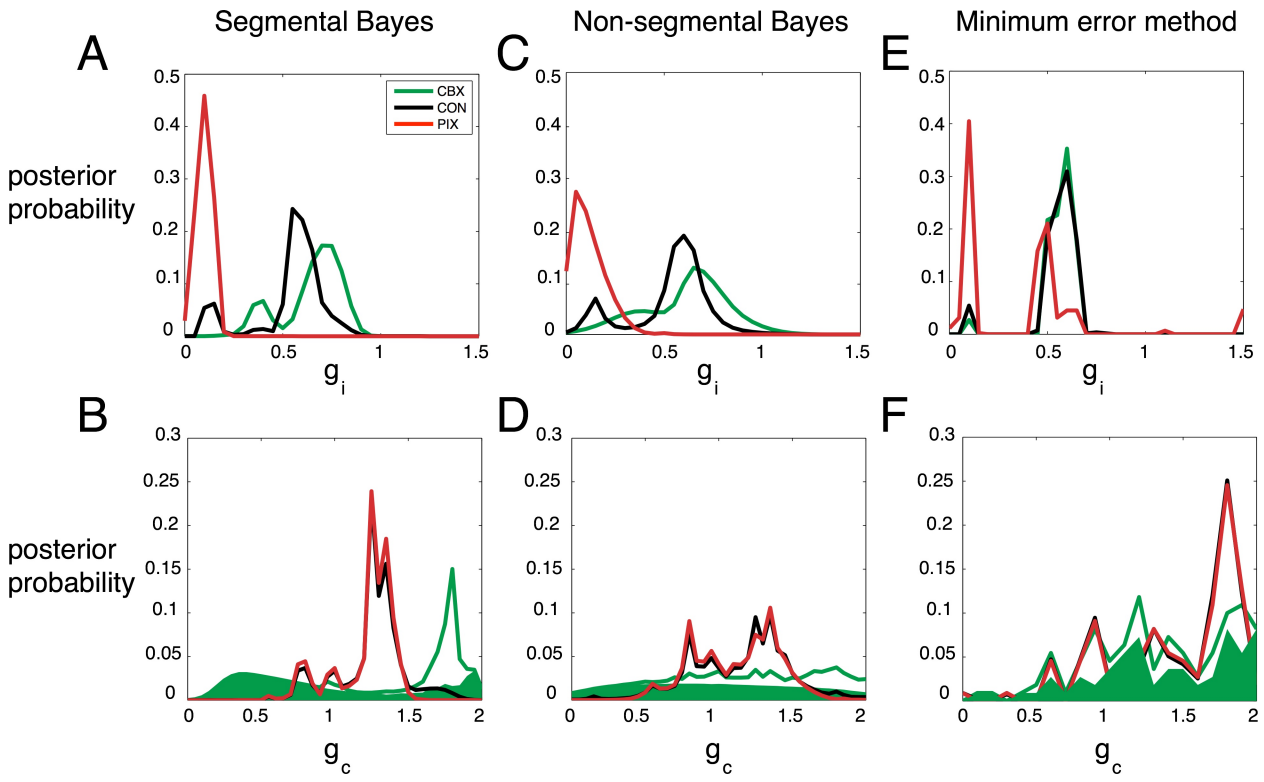

Figure 5-6: Estimates for the entire IO neuronal population

A-B: the average g_i and g_c estimates by the segmental Bayesian inference for the entire IO neuronal population. C-D: those similar to A and B but by non-segmental Bayesian inference where the posterior probability was estimated across the entire spike train of the individual IO neurons. E-F: estimates by the minimum-error method. Filled and open areas in green in B, D and F represent the estimates for the two different animals in the CBX condition.

the minimum error method), PIX (0.1±0.04, 0.38±0.32 mS/cm^2) and CBX conditions (0.65±0.15, 0.56±0.08 mS/cm^2), and the g_c for the CBX condition (1.24±0.6 and 1.36±0.46 mS/cm^2). Those of disagreement were the g_c for the CON and PIX conditions (1.21±0.2 and 1.47±0.43 mS/cm^2).

5.5 Robustness of the segmental Bayes

We hypothesize that the segmental Bayes minimizes the errors of g_i and g_c estimation because of the failure for the forward model to reproduce the non-stationary dynamics of IO firing. This hypothesis was tested by comparing the performance of the segmental and non-segmental Bayes in terms of the PCA error rate (the difference in the PCA scores between the EXP and the corresponding SIM spikes that were generated by the g_i and g_c estimated for those EXP spikes). PCA errors for the segmental Bayes were smaller than the non-segmental Bayes across the three experimental conditions ($F = 14.18$, $p = 0.0002$), the difference being most significant for PIX, less for CON, and insignificant for CBX (cf. solid and hatched columns Figure 5-7A). Correspondingly, the non-stationarity of the EXP spikes estimated as the Kolmogorov-Smirnov (KS) difference between the distribution of the inter-spike intervals for the EXP spikes and that of Poisson and the standard deviations of the firing rate ranked in the same order as that for the significance of the PCA error difference between the segmental and non-segmental Bayes, being high, medium and low for the PIX, CON and CBX conditions (cf. Figures 5-7A with C and D), respectively. These findings are consistent with our view that the segmental Bayes minimizes errors in g_i and g_c estimates because of the non-stationary dynamics of IO firing. It is notable that the corresponding SIM spikes rather faithfully reproduced the non-stationarity of the EXP spikes for the two measures across the three experimental conditions, while they were significantly smaller for the LV (Figure 5-7B). This finding indicates that the present simulation failed to precisely reproduce the non-stationarity estimated by the LV.

Finally, we confirmed the superiority of the segmental Bayesian inference over the minimum error method used in our previous study [49] in terms of the PCA error rate.

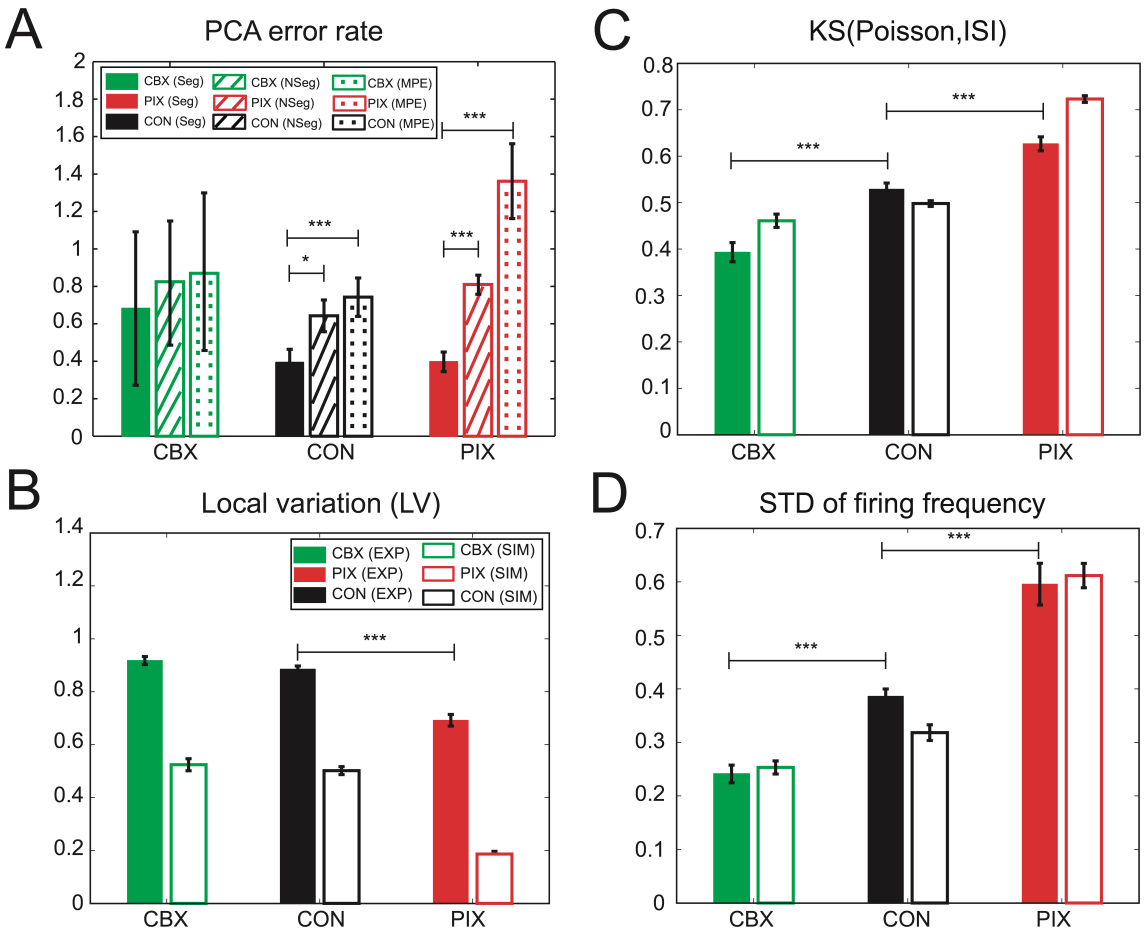

Figure 5-7: Performance of the segmental and non-segmental Bayesian inference and the minimum PCA error method and the non-stationarity of EXP and SIM spike data

A: PCA error rates of the g_i and g_c estimates for the segmental (solid columns, Seg) and non-segmental (hatched, NSeg) Bayesian inference and the minimum PCA error method (dotted, MPE) averaged for the entire IO neurons for CBX, CON and PIX conditions. The colors represent the three experimental conditions and the texture patterns represent the errors for the three methods of g_i and g_c estimates. B-D: Non-stationality of the spike data estimated as the three metrics. B: LV; C: KS distance of the ISI distribution for the EXP (solid columns) and SIM (blank) spike data from Poisson distribution; D: standard deviation of the instantaneous firing rate. The colors represent the three experimental conditions and the texture patterns represent EXP and SIM data.

The magnitude of the error rate was smaller for the segmental Bayesian inference (solid columns in Figure 5-7A) than that for our previous study (dotted columns) across the three experimental conditions (statistical significance, F = 23.37, p < 0.0001 by ANOVA), and the statistical significance of the error rate was largest (p < 0.0001 by t-test), moderate (p < 0.01) and minimum (p > 0.7) for the PIX, CON and CBX conditions, respectively, corresponding to the degree of the non-stationarity of the EXP spikes. It is notable that the average number of mixed Gaussians per (g_i, g_c) grid of the forward models was three orders of magnitude smaller in the segmental Bayes (n = 8.55) than that in our previous study (n = 12,600) and slightly larger than that for the non-segmental Bayesian inference (n = 2.3), indicating that there was over- and under-fitting in the previous study and the non-segmental Bayesian inference, respectively, compared with the segmental Bayesian inference used in the present study.

5.6 Discussions

The goal of the present thesis was to resolve the inverse problem estimating the two important parameters of the IO network (i.e., g_i and g_c) by fitting the firing dynamics of the model network with those of the IO network. The parameter estimation was confronted with a huge mismatch of the model network with the brain network in the system complexity such as the granularity, the hierarchy, the degrees of freedom and the non-stationary dynamics. Consequently, the inverse problem becomes severely ill-posed [52, 1], and necessitates some stochastic approaches that find the most likely solution among many possible ones according to various error functions [13].

In [49], we defined the error function as the distance between the experimental and corresponding simulation spike data in the PCA space (PCA error), constructed of various feature vectors (FVs) that are derivatives of the ISIs of the experimental spike data such as the firing rate, the auto- and cross correlation, the minimum distance (MD), the spike distance (SD), and the local variance (LV), representing the spatiotemporal firing dynamics and contained strong redundancy. In that study,

the FVs were determined for short spike segments (50s) to compensate for the non-stationarity of the experimental spike trains [15, 54], PCA was conducted to remove the redundancy, and the g_i and g_c were determined as the ones giving the minimum PCA errors to the experimental spike segments. The minimum error method can be regarded as the extreme case of Bayesian inference where the forward model translating the model parameters into the spike features was constructed for each spike segment. This approach is equivalent to assuming different Gaussians (i.e., parameter-spike feature translation mechanisms) for every spike segment of the same single neuron and may be regarded as over-fitting.

A recent study [18] maintained the segmental approach and corrected the over-fitting by the hierarchical Bayesian inference that estimated the g_i and g_c by fitting Gaussians to every spike segment and merged them into single g_i and g_c estimate according to the neuronal constraint that assumes the same g_i and g_c for a single neuron (Figures 5-4 and 5-5). This view is supported by the fact that the number of Gaussians used for construction of the forward model is three orders of magnitude smaller for the present segmental Bayesian inference than that for the minimum error method. The segmental Bayes could be regarded as a way to minimize estimation errors of g_i and g_c due to the errors of the current forward model to precisely reproduce the non-stationality of IO firing. Allowance of fluctuations for segmental g_i and g_c estimates is equivalent to recent methods [24, 20] to reduce parameter estimation errors due to modeling errors by assuming system noise.

The overall performance of the segmental Bayesian inference estimated as the PCA error that is the distance between the experimental and corresponding simulation spike segments in the PCA space was generally higher across the three experimental conditions than those for the minimum PCA error method and the non-segmental Bayesian inference that estimated the g_i and g_c across the entire spike length (Figure 5-7A). The statistical significance of the difference was high, modest and minimal in the PIX, CON and CBX conditions, respectively, in correspondence with the non-stationarity of the IO firing evaluated as the three metrics, including the KS distance of the ISIs from Poisson distributions, the LV, and the standard deviation of the

firing rate (Figures 5-7B-D). These findings indicate that segmental Bayesian inference performs better than the other two methods in cases of highly non-stationary firing dynamics.

Experimental evidence for the coupling modulation from inhibition from DCN was previously reported [7]. We found that g_i was roughly decreased 80% under PIX condition. Under simplified assumptions, the effective coupling conductance g_{eff} between two neighboring IO cells was computed from the spine neck conductance g_{spine}, inhibitory conductance g_i and gap-junctional conductance g_c as follows [26]

$$g_{eff} = (g_{spine} \times g_c)/(g_c + g_{spine} + g_i) \tag{5.1}$$

As a result, PIX increased 30% of g_{eff} due to inhibition block. That was consistent with previous studies [26, 49] supporting the direct role of inhibition input in modulation of coupling strength. Since the inhibition originated from DCN, the strength of the coupling and thus the oscillatory and synchronous activities displayed by IO cells presumably depends on the modulation of DCN via plastic processes in the cerebellar cortex and the nuclei. From that viewpoint, the PC-DCN-IO triangle may act to realize such modulation scheme in two phases of cerebellar learning as follows. In the early phase, the motor commands are strongly disturbed and far from desired ones. A strong coupling allows a widespread synchrony among IO activities and potentially lead to a massive change in the weights of parallel fiber-Purkinje cell synapses, resulting a fast but coarse learning in the cerebellar cortex. Inversely, in the late phase of learning, as the motor error is small, the PC activities become weak and occur in only a restricted group of PCs. The inhibited PCs activate the neurons in the nuclei and, as a consequence, the excited DCN release strong GABAergic signal to decrease the coupling between IO cells via shunting inhibition for only fine tunes in motor commands, resulting a sophisticated learning. In [64], we examined the idea of adaptive coupling in cerebellar learning and found that such a decrease in coupling strength can be beneficial for motor learning, since efficient coupling strength depends upon the magnitude of the error signals.

Chapter 6

Conclusions

6.1 Summary

Rapid progress in computer science now enables simulations of neuronal networks with high complexity. Advanced technology in neuroscience enables sampling of a massive amount of neuronal data from the brain. Combining technologies across two fields of science to understand the computations in the brain still face severe difficulties mainly because of the fact that the technologies of both fields are still rather simplistic compared to a huge complexity of the brain network. It is nevertheless a big challenge in computational neuroscience to construct a brain model that simulates brain computations.

Modeling of the brain requires to constraint number of model parameters, which are typically hand-tuned by experts. This process is time consuming and restrictive. Estimation of the model parameters directly from the observed neuronal activity is thus desired. Traditionally, parameter estimation of quantitative model utilizing experimental data has been investigated in relatively well-defined situations where hierarchy, granularity and degrees-of-freedom of the experimental data, the quantitative model and the parameters to be estimated are similar. If they are not matched well with each other, parameter estimation problems are considered impossible to solve, or at least severely ill-posed. For example, estimating ionic conductance of some active channels in a compartment model of Purkinje cells while reproducing temporal wave-

forms of intracellular membrane potential belongs to the former class since the model, measured data and estimated parameters all belong to a single-cell intracellular level of hierarchy. However, the current problem to estimate two conductance values of an IO network of compartment-model neurons based on spike timings of a number of neurons belongs to the latter class for the following reasons. First, the experimental data is at a network level while the estimated parameters are at a synapse level and they are far apart in brain hierarchy. Second, the IO network of compartment-model neurons are far more complicated and have larger degrees of freedom compared with the experimental data and estimated parameters. Third, because of the complexity of the real IO network, we cannot expect that the simple network model can perfectly reproduce the observed experimental data. Overall, there is no simple one-to-one mapping between the experimental data and the estimated parameters. Apparently, a class of estimation algorithms, which are characterized as deterministic methods, is not well suited to the current problem, and in a broader sense, the latter class of severely ill-posed estimation problems.

The primary goal of our study is to estimate the two parameters, gap junctional (g_c) and inhibitory (g_i) conductance, from the IO spike data sampled under three experimental conditions (CON, PIX and CBX). We constructed 3×3 neuronal network model and simulated firing of IO networks by changing g_i and g_c by 0.05 steps for a range of [0–1.5 mS/cm^2] and [0–2.0 mS/cm^2], respectively. We evaluated the firing dynamics of EXP and SIM spike data using sixty-eight FVs including firing frequency, local variation, auto- and cross-correlogram, minimal distance and spike distance. The FVs were rated by the mutual information that the FVs of SIM spike data conveyed concerning g_i and g_c and the top twenty-five FVs were selected for principal component analysis (PCA). The first three PCA components, which together account for 55% of the total variance, were extracted for construction of the forward model of Bayes. We confirmed that the distribution of SIM spike data in the 3-dimensional PCA space completely covers that of the EXP one. The likelihood function was estimated as the Gaussian mixture model in PCA space based on the SIM data.

The Bayesian approach to estimate g_i and g_c from the spike data contains the two theoretical difficulties. The first one was that the IO neuronal cross-talk controlling the firing dynamics depends on the ratio rather than the individual values of g_i and g_c. The second one was that IO firing conveys complicated dynamics that are difficult to be precisely reproduced by the simulation model. We resolved the first difficulty by the hierarchical Bayes approach introducing the commonality constraint that g_c estimate for PIX spike data equals to that for CON spike data and that g_i estimate for CBX spike data equals to that for CON spike data. The second difficulty was resolved by the segmental Bayes approach that finds an estimate for each spike segment rather than the entire spike data, and finally finds a single estimate with a Gaussian scatter that fits to the ensemble of the segmental estimates. The variation of the segmental estimates due to the complicated dynamics of IO firing may be cancelled out by the Gaussian fitting. We studied the effects of the commonality constraint by comparing the estimates under the regular and relaxed commonality constraint, and found that the posterior probability becomes much shaper for the Bayes with the regular than relaxed commonality constraint. We also investigated the performance of the segmental, non-segmental Bayes, which finds the estimates once across the entire spike data, and minimum-error method, which directly finds the closest match in the feature space, by evaluating the PCA error for every g_i and g_c estimate of the IO neurons, as the difference of the PCA scores between the EXP spike from which those g_i and g_c were estimated and the SIM spike that were generated from those g_i and g_c. They were referred to the non-Poisson and non-stationary dynamics of the EXP spike data, estimated as LV, KS divergence and STD of the firing rate for PIX, CBX and CON conditions. PCA errors of the segmental Bayes were consistently smaller than those of non-segmental Bayes and minimum error method for all of the three experimental conditions. The statistical significance paralleled with the estimates of the non-Poisson and non-stationality of firing. The posterior probability of g_i and g_c for the entire ensemble of the IO neurons showed that g_i was low, medium and high, and conversely g_c was high, medium and low for PIX, CON and CBX conditions, respectively. These findings are consistent with those of the neuroscience that PIX

and CBX depress g_i and g_c, respectively. More specifically, PIX reduced 80% of g_i whereas CBX decreased 10% g_c from CON level, supporting the hypothesis that inhibitory input from DCN is a control mechanism of the oscillatory and synchronous IO activity.

To further demonstrate its usability, validation of the previously developed approaches was conducted. By adopting the same task of estimating two conductance values in the inferior olive network model, we used simulated spike data as the test data. In contrast to the experimental data, the simulation data are suitable for the validation purpose because the true parameter values are known. Performance evaluation on the test data confirmed that the segmental Bayesian inference provides smaller estimation errors than the conventional Bayesian inference or the minimum error methods. Robustness of the segmental Bayesian approach against highly non-stationary dynamics of the spike data was also observed. All of these findings indicated that the segmental Bayes with the commonality constraint is useful means to derive reliable estimates overcoming the difficulty of the complicated firing dynamics and ill-posed problem.

6.2 Contributions

Modeling is a significant task to understand how the brain works even at different levels of granularity and computational abstraction. Our studies contribute to the field of computational modeling by developing an advanced model of the IO neurons, powerful methods for data analysis that is able to capture the structure of statistical dependence of IO network activity across neurons and time, and a novel framework for resolving the parameter estimation despite the imperfectness of the model. Those three major contributions of the present thesis are specifically described as follows.

- Most importantly, we successfully developed a stochastic approach based on the Bayesian inference to resolve the inverse problem of estimating model parameters from spike trains with complicated firing dynamics. There are obviously several reasons for the system mismatch between the brain and the model,

such as the degree-of-freedoms, the granularity-hierarchy as well as the non-stationarity. This huge mismatch inevitably results in modeling errors. To compensate those errors, the segmental Bayes allows segmental fluctuations in the parameter estimates and merges the estimates for a single neuron with the neuronal constraint. It has been shown to significantly reduce the estimation errors in both experimental and simulation data, and also has a strong robustness against the non-stationarity of the spike data. We thus argue that the segmental Bayes is a useful tool to evaluate parameters of interest for neuroscience from experimental spike train data.

- Second, the network model consisting of nine compartmental-detailed neurons developed in our study is the most realistic model of inferior olive neurons to date. To the best of our knowledge, there has yet to be an IO model with spines. The model allows us to investigate the origin of IO firing dynamics even at the synapse level, specifically, how the interactions between gap-junctional (g_c) and inhibitory (g_i) synaptic signals shape IO spiking patterns.

- Third, we also proposed a plausible procedure to characterize important features of the spike data. The spatiotemporal firing dynamics of the spike data were evaluated using a set of sixty-eight features. The mutual information of the feature vectors and the parameter space was conducted to retain rich-information features and eliminate poor-information ones. The principal component analysis was also applied to further remove the redundancy among those features. This three-step procedure allows us to extract compact but still informative feature vectors of the spike data.

As a final remark, we note that many of the techniques developed in this work are not limited to the narrow context of inverse problems. For instance, it has been shown that the stochasticity in the parameter space may have an effect to compensate for the modeling errors, because the fluctuations in the parameter space can be translated into those in any observation space (e.g., ion channel currents, membrane potentials, spike trains, etc.) by simple mathematical transformation [24, 20].

Thus, the segment-wise methodology can be applied to effectively constraint model parameters to the experimental data collected by various electrophysiological techniques, such as the multiple electrode arrays, optical recording using various dyes, and optogenetic techniques [51, 48]. Alternatively, the simulation model constructed in our study can be utilized to study the synchronization of the network of coupled neurons, in which the electrical coupling via gap junctions determines the oscillatory and synchronous neuronal activities [5, 72]. Our proposed procedure to extract the spatio-temporal features of the multiple neural spike train data can be also applied to identify spike events in spike sorting or other spike pattern classification methods [39, 60]. Therefore, although the framework was developed to motivate the parameter estimation, its usability is likely to transcend beyond that specific problem.

6.3 Future works

Many attempts have been made to create accurate computer models of distinct parts of the brain. Still, the difference between predictions of the models and the brain observables is usually inevitable due to practical challenges. For instance, despite its most advanced structure, the IO network model in our studies consists of nine neurons, which are three orders of magnitude smaller than in real IO network. Indeed, we only constrained two parameters of interest and fixed other parameters as simulating the spike data. The degrees of freedom of the model are thus far smaller than that of the brain. One of our future tasks is to develop a more sophisticated model to bridge the gap in the system complexity between the brain and the model. Among several available approaches, increasing the number of simulated neurons and adding new features that characterize the neuronal firing dynamics seem to be plausible and efficient.

The second option of our future works arises from the fact that the experimental data of IO neurons used in our previous studies possess two severe limits: the number of recorded neurons was quite small and its neural network structure was unknown. Those limitations intensely cause restrictions of exploring neuronal in-

teractions among IO cells within or across cerebellar micro-zones. Here, different micro-zones correspond to various functional modules of the cerebellum. To tackle this issue, we aimed to utilize other experimental data sets which were collected by a state-of-the-art recording technique, namely, two-photon imaging. The two-photon imaging can track, *in vivo*, Calcium concentration activities of hundreds of Purkinje cells in different cerebellar micro-zones, and provides plentiful neural information for our analysis of IO firing. The next task is thus to extend our previous studies based on newly available two-photon data, more specifically, to estimate the gap-junctional conductance under different conditions and/or different anatomical loci. Furthermore, computational modeling of cerebellar learning and control based on these estimations will be a pioneering work in this research field.

Appendix A

Compartmental model of Inferior olive neurons

The membrane potential of the soma, dendrite, and spine compartments (V_o, V_d and V_p) was calculated by

soma:

$$C_m \frac{dV_o}{dt} = -\sum I_{Na} + I_K + I_{Cal} + I_h + I_{lo} + I_{do} + I_{synapse} \tag{A.1}$$

dendrite:

$$C_m \frac{dV_d}{dt} = -\sum I_{CaH} + I_{KCa} + I_{od} + I_{ld} + \sum_{i=1}^{4} I_{pd} + I_{synapse} \tag{A.2}$$

spine:

$$C_m \frac{dV_p}{dt} = -\sum I_C + I_{lp} + I_{dp} + I_{synapse} \tag{A.3}$$

A.1 Soma compartment

The structures of the soma compartment exactly followed those of [59]. The change of somatic membrane potential V_o, which is proportional to the sum of I_{Na}, I_K, I_{Cal}, I_h, I_{lo}, I_{do}, and $I_{synapse}$ that consists of I_e and I_i, as follows

soma:

$$C_m \frac{dV_o}{dt} = -\sum I_{Na} + I_K + I_{Cal} + I_h + I_{lo} + I_{do} + I_{synapse}$$

where C_m is the membrane capacitance $1 micro F/cm2$, and I_{Na}, I_K, I_{Cal}, I_h, I_{do}, and $I_{synapse}$ are the currents across ionic conductances g_{Na}, g_K, g_{Cal}, g_h, g_o, g_e and g_i. The parameter values used in the simulation are summarized in Table A.1. I_{Na} is given by the Hodgkin-Huxley type inward sodium current as

$$\begin{aligned}
&I_{Na} = g_{Na} m_\infty^3 h (V_o - V_{Na}) \\
&m_\infty(V_o) = \frac{\alpha_m(V_o)}{\alpha_m(V_o) + \beta_m(V_o)} \\
&\alpha_m(V_o) = \frac{0.1(V_o + 41)}{1 - \exp\left[-\frac{V_o+41}{10}\right]} \qquad \beta_m(V_o) = 9.0 \exp\left[-\frac{V_o + 66}{20}\right] \\
&h_\infty(V_o) = \frac{\alpha_h(V_o)}{\alpha_h(V_o) + \beta_h(V_o)} \qquad \tau_h(V_o) = \frac{170}{\alpha_h(V_o) + \beta_h(V_o)} \\
&\alpha_h(V_o) = 5.0 \exp\left[-\frac{V_o + 60}{15}\right] \qquad \beta_h(V_o) = \frac{V_o + 50}{1 - \exp\left[-\frac{V_o+50}{10}\right]}
\end{aligned} \tag{A.4}$$

Outward delayed rectifier potassium current I_K is described by

$$\begin{aligned}
&I_K = g_K n^4 (V_o - V_K) \\
&n_\infty(V_o) = \frac{\alpha_n(V_o)}{\alpha_n(V_o) + \beta_n(V_o)} \qquad \tau_n(V_o) = \frac{5}{\alpha_n(V_o) + \beta_n(V_o)} \\
&\alpha_n(V_o) = \frac{V_o + 41}{1 - \exp\left[-\frac{V_o+41}{10}\right]} \quad \beta_n(V_o) = 12.5 \exp\left[-\frac{V_o + 51}{80}\right]
\end{aligned} \tag{A.5}$$

Low-threshold calcium inward current I_{Cal} is described by

$$\begin{aligned}
&I_{Cal} = g_{Cal} k^3 l (V_o - V_{Ca}) \\
&k_\infty(V_o) = \frac{1}{1 + \exp\left[-\frac{V_o+61}{4.2}\right]} \qquad \tau_k(V_o) = 1.0 \\
&l_\infty(V_o) = \frac{1}{1 - \exp\left[\frac{V_o+85.5}{8.5}\right]} \quad \tau_l(V_o) = \frac{20 \exp\left[\frac{V_o+160}{30}\right]}{1 + \exp\left[\frac{V_o+84}{7.3}\right]} + 35
\end{aligned} \tag{A.6}$$

Anomalous inward rectifier current I_h is described by

$$\begin{aligned} I_h &= g_h q(V_o - V_h) \\ q_\infty(V_o) &= \frac{1}{1+\exp\left[-\frac{V_o+75}{5.5}\right]} \quad \tau_q(V_o) = \frac{1}{\exp(-0.086V_o - 14.6) + \exp(0.07V_o - 1.87)} \end{aligned} \tag{A.7}$$

Leakage current I_{lo} is described by

$$I_{lo} = g_o(V_o - V_l) \tag{A.8}$$

Current I_{do} flowing from the dendritic compartment to the somatic compartment is given by

$$I_{do} = g_{do}(V_o - V_d) = \left(\frac{G^{soma,dendrite}}{p} \cdot s\right)(V_o - V_d) \tag{A.9}$$

Here, $G^{soma,dendrite}$ is the actual soma-dendritic inter-compartmental conductance in mS. s is the total surface area of a single neuron. The value of $G^{soma,dendrite}$ is given in Table A.1.

A.2 Dendritic compartment

The structure of the dendritic compartment was the same as Schweighofer's model except that the gap junction was moved to the spine compartment, and its membrane potential (V_d) obeys the following differential equation:

$$C_m \frac{dV_d}{dt} = -\sum I_{CaH} + I_{KCa} + I_{od} + I_{ld} + \sum_{i=1}^{4} I_{pd} + I_{synapse}$$

High-threshold inward calcium current I_{Cah} through g_{Cah} is given by

$$\begin{aligned} I_{Cah} &= g_{Cah} r^2 (V_d - V_{Ca}) \\ r_\infty(V_d) &= \frac{\alpha_r(V_d)}{\alpha_r(V_d) + \beta_r(V_d)} \quad \tau_r(V_d) = \frac{1}{\alpha_r(V_d) + \beta_r(V_d)} \\ \alpha_r(V_d) &= \frac{1.6}{1+\exp\left[-\frac{V_d-5}{13.9}\right]} \quad \beta_r(V_d) = \frac{0.02(V_d+8.5)}{\exp\left[\frac{V_d+8.5}{5}\right]-1} \end{aligned} \tag{A.10}$$

Outward calcium-dependent potassium current I_{KCa} through g_{KCa} is given by

$$
\begin{aligned}
&I_{KCa} = g_{KCa} r^2 (V_d - V_K) \\
&s_\infty([Ca^{2+}]) = \frac{\alpha_s([Ca^{2+}])}{\alpha_s([Ca^{2+}]) + \beta_s([Ca^{2+}])} \quad \tau_s([Ca^{2+}]) = \frac{1}{\alpha_s([Ca^{2+}]) + \beta_s([Ca^{2+}])} \\
&\alpha_s([Ca^{2+}]) = \min 0.00002[Ca^{2+}], 0.01 \qquad \beta_s([Ca^{2+}]) = 0.015 \\
&\frac{ds}{dt} = \frac{s_\infty([Ca^{2+}] - s)}{\tau_s([Ca^{2+}])} \\
&\frac{d[Ca^{2+}]}{dt} = I_{Cah} - 0.02[Ca^{2+}]
\end{aligned}
\tag{A.11}
$$

Leakage current I_{ld} through g_d is given by

$$I_{ld} = g_d(V_d - V_l) \tag{A.12}$$

The inter-compartmental current flowing from the somatic compartment to dendritic compartment I_{od} is given by

$$I_{od} = g_{od}(V_d - V_o) = \left(\frac{G^{soma,dendrite}}{1 - p - q} \cdot s \right) (V_d - V_o) \tag{A.13}$$

where p is the ratio of the somatic area to the total surface area and q is the ratio of the total of the four spine surface area to the total surface area. The inter-compartmental current flowing from the i-th ($i = 1, 2, 3, 4$) spine compartment to dendritic compartment I_{pd} is given by

$$[I_{pd}]_i = g_{pd} \left(V_d - [V_p]_i\right) = \left(\frac{G^{dendrite,spine}}{1 - p - q} \cdot s \right) (V_d - [V_p]_i) \tag{A.14}$$

A.3 Spine compartment

The spine compartment is added in our IO neuron model. In the spine compartment, the IO neurons lie next to each other and are coupled by I_C as follows:

$$C_m \frac{dV_p}{dt} = -\sum I_C + I_{lp} + I_{dp} + I_{synapse}$$

The current flowing into other cells through electrical coupling I_C is given by

$$[I_C]_i = g_c \left([V_p]_i - V_{p_{next}} \right) \tag{A.15}$$

Leakage current I_{lp} is described by

$$[I_{lp}]_i = g_p \left([V_p]_i - V_l \right) \tag{A.16}$$

The inter-compartmental current flowing from one of the spine compartments to dendritic compartment I_{dp} is given by

$$[I_{dp}]_i = g_{dp} \left([V_p]_i - V_d \right) = \left(\frac{G^{dendrite,spine}}{0.25q} \cdot s \right) \left([V_p]_i - V_d \right) \tag{A.17}$$

A.4 Synaptic Inputs

All of the soma, dendritic, and spine compartments receive the excitatory and inhibitory synaptic inputs driven by the Poisson spike generators of the mean firing rate 10 Hz. The number of excitatory and inhibitory synapses are 10, 80, and 10 for the soma, dendrite, and spine compartments, respectively, driven by Poisson process spike generators defined as

$$\begin{aligned} I_{syn}(t) &= \sum_l g_{syn}(t - t_l)(V - E_{syn}) \\ g_{syn}(t) &= \begin{cases} 0 \\ g_{synm} \cdot t \cdot e^{1 - t/t^{peak}} \end{cases} \end{aligned} \tag{A.18}$$

where t_l is the time of the l-th spike time, $E_{syn} = -10mV$ or $-75mV$, and $g_{syn} = g_e$ or g_i for the inhibitory and excitatory synapses, respectively. The hyperpolarizing constant current of Schweighofer's model was replaced by the inhibitory synaptic inputs in our model.

A.5 Parameters of the compartmental model

Parameter	Value	References
g_{Na}	70.0 mS/cm^2	[59]
g_K	18.0 mS/cm^2	[59]
g_{Cal}	2.0 mS/cm^2	[58]
g_h	0.15 mS/cm^2	[58]
g_s	0.015 mS/cm^2	[59]
g_{Cah}	4.0 mS/cm^2	[59]
g_{KCa}	35.0 mS/cm^2	[59]
g_d	0.015 mS/cm^2	[59]
g_p	0.015 mS/cm^2	[59]
g_e	0.03 mS/cm^2	[58]
$G^{soma,dendrite}/S$	0.13 mS/cm^2	[59]
$G^{dendrite,spine}/S$	0.1 mS/cm^2	$g_{sd} = 0.1 - 3$ in [59], $g_{dp} \leq g_{sd}$
V_{Na}	$55mV$	[59]
V_K	$-75mV$	[59]
V_{Ca}	$120mV$	[59]
V_h	$-43mV$	[59]
V_l	$10mV$	[59]
p	0.14	The ratio of the somatic area to total surface area 0.1-0.4
q	0.05	

Table A.1: Simulation parameters of the compartmental model

Bibliography

[1] P. Achard and E. De Schutter. Complex parameter landscape for a complex neuron. *PLoS Computational Biology*, 2(7), 2006.

[2] J. S. Albus. A theory of cerebellar function. *Mathematical Biosciences*, 10(25-61), 1971.

[3] S.R. Arridge, J. S. Kaipio, V. Kolehmainen, M. Schweiger, E. Somersalo, T. Tarvainen, and M. Vauhkone. Approximation errors and model reduction with an application in optical diffusion tomography. *Inverse Problems*, 22(1):175–196, 2006.

[4] B. Aslan and G. Zech. Statistical energy as a tool for binning-free, multivariate goodness-of-fit tests, two-sample comparison and unfolding. *Nuclear Instruments and Methods in Physics Research Section A*, 537(3):626–636, 2005.

[5] M. V. Bennett and R. S. Zukin. Electrical coupling and neuronal synchronization in the mammalian brain. *Neuron*, 41:495–511, 2004.

[6] R. W. Berg and S. Ditlevsen. Synaptic inhibition and excitation estimated via the time constant of membrane potential fluctuations. *Journal of Neurophysiology*, 110:1021–1034, 2013.

[7] A. R. Best and W. G. Regehr. Inhibitory regulation of electrically coupled neurons in the inferior olive is mediated by asynchronous release of gaba. *Neuron*, 62(4):555–565, 2009.

[8] C. M. Bishop. *Pattern recognition and machine learning*. Springer, 2006.

[9] T. A. Blenkinsop and E. J. Lang. Block of inferior olive gap junctional coupling decreases purkinje cell complex spike synchrony and rhythmicity. *The Journal of Neuroscience*, 26(6):1739–1748, 2006.

[10] E. Brown, R. Kass, and P. Mitra. Multiple neural spike train data analysis: state-of-the-art and future challenges. *Nature Neuroscience*, 7:456–461, 2004.

[11] S. Druckmann, Y. Banitt, A. Gidon, F. Schurmann, H. Markram, and I. Segev. A novel multiple objective optimization framework for constraining conductance-based neuron models by experimental data. *Frontiers in Neuroscience*, 1(1):7–18, 2007.

[12] D. Fairhurst, I. Tyukin, H. Nijmeijer, and C. Van Leeuwen. Observers for canonic models of neural oscillators. *Mathematical Modelling of Natural Phenomena*, 5(2):146–184, 2010.

[13] W. Van Geit, E. De Schutter, and P. Achard. Automated neuron model optimization techniques: a review. *Biological Cybernetics*, 99:241–251, 2008.

[14] P. F. Gilbert and W. T. Thach. Purkinje cell activity during motor learning. *Brain Research*, 128(2):309–328, 1977.

[15] S. Grun, M. Diesmann, and A. Aertsen. Unitary events in multiple single-neuron spiking activity. ii. nonstationary data. *Neural Computation*, 14:81–119, 2002.

[16] Y. Hirata and K. Aihara. Representing spike trains using constant sampling intervals. *Journal of Neuroscience Methods*, 183:277–286, 2009.

[17] H. Hoang and I. T. Tokuda. Validation of the minimum-error method for estimating model parameters from neural spike train data. *Journal of Signal Processing*, 19(4):(in press), 2015.

[18] H. Hoang, O. Yamashita, I.T. Tokuda, M. Kawato, M. Sato, and K. Toyama. Segmental bayesian estimation of gap-junctional and inhibitory conductance of io neurons from spike trains with complicated dynamics. *Frontiers in Computational Neuroscience*, 9(56), 2015.

[19] G.J. Hoge, K.G.V. Davidson, T. Yasumura, P.E. Castillo, J.E. Rash, and A.E. Pereda. The extent and strength of electrical coupling between inferior olivary neurons is heterogeneous. *J. Neurophysiol.*, 105:1089–1101, 2011.

[20] J. Huttunen and J. Kaipio. Approximation errors in nonstationary inverse problems. *Inverse Problems and Imaging*, 1(1):77–93, 2007.

[21] K. Ikeda, K. Otsuka, and K. Matsumoto. Maxwell-bloch turbulence. *Progress of Theoretical Physics, Supplement*, 99:295–324, 1989.

[22] M. Ito. Experimental verification of marr-albus plasticity assumption for the cerebellum. *Acta biologica Academiae Scientiarum Hungaricae*, 33(189-199), 1982.

[23] M. Ito. *The cerebellum and neural control*. Raven Press, 1984.

[24] J. Kaipio and E. Somersalo. Statistical inverse problems: Discretization, model reduction and inverse crimes. *Journal of Computational and Applied Mathematics*, 198:493–504, 2007.

[25] K. Kaneko. Clustering, coding, switching, hierarchical ordering, and control in a network of chaotic elements. *Physica D*, 41:137–172, 1990.

[26] Y. Katori, E. J. Lang, M. Onizuka, M. Kawato, and K. Aihara. Quantitative modeling of spatio-temporal dynamics of inferior olive neurons with a simple conductance-based model. *International Journal of Bifurcation and Chaos*, 20(2010):583–603, 2010.

[27] M. Kawato, K. Furukawa, and R. Suzuki. A hierarchical neural-network model for control and learning of voluntary movement. *Biological Cybernetics*, 57:169–185, 1987.

[28] M. Kawato and H. Gomi. A computational model of four regions of the cerebellum based on feedback-error learning. *Biological Cybernetics*, 68:95–103, 1992.

[29] M. Kawato, S. Kuroda, and N. Schweighofer. Cerebellar supervised learning revisited: biophysical modeling and degrees-of-freedom control. *Current Opinion in Neurobiology*, 21:1–10, 2011.

[30] N. Keren, N. Peled, and A. Korngreen. Constraining compartmental models using multiple voltage recordings and genetic algorithms. *Journal of Neurophysiology*, 94:3730–3742, 2005.

[31] S. Kirkpatrick, C. D. Gelatt Jr, and M. P. Vecchi. Optimization by simulated annealing. *Science*, 220(4598):671–680, 1983.

[32] S. Kitazawa, T. Kimura, and P. B. Yin. Cerebellar complex spikes encode both destinations and errors in arm movements. *Nature*, 392(6675):494–497, 1998.

[33] J. Kitazono, T. Omori, T. Aonishi, and M. Okada. Estimating membrane resistance over dendrite using markov random field. *IPSJ Trans. Mathematical modeling and its applications*, 5:89–94, 2012.

[34] C. Koch and I. Segev. *Methods in neuronal modeling: from ions to networks*. Cambridge, MA, MIT Press, 2nd edition, 1998.

[35] T. Kreuz, D. Chicharro, C. Houghton, R.G. Andrzejak, and F. Mormann. Monitoring spike train synchrony. *J. Neurophysiol.*, 109:1457–1472, 2013.

[36] E. J. Lang. Gabaergic and glutamatergic modulation of spontaneous and motor-cortex-evoked complex spike activity. *Journal of Neurophysiology*, 87:1993–2008, 2002.

[37] E. J. Lang, I. Sugihara, and R. Llinas. Gabaergic modulation of complex spike activity by the cerebellar nucleoolivary pathway in rat. *Journal of Neurophysiology*, 76:255–275, 1996.

[38] P. Lansky and S. Ditlevsen. A review of the methods for signal estimation in stochastic diffusion leaky integrate-and-fire neuronal models. *Biological Cybernetics*, 99:253–262, 2008.

[39] M. S. Lewicki. A review of methods for spike sorting: the detection and classification of neural action potentials. *Network: Computation in Neural Systems*, 9(4):R53–R78, 1998.

[40] R. Llinas, R. Baker, and C. Sotelo. Electrotonic coupling between neurons in cat inferior olive. *Journal of Neurophysiology*, 37:560–571, 1974.

[41] R. Llinas and Y. Yarom. Electrophysiology of mammalian inferior olivary neurones in vitro. different types of voltage-depedent ionic conductances. *J. Physiol.*, 315:549–567, 1981.

[42] Z. F. Mainen, J. Joerges, J. R. Huguenard, and T. Sejnowski. A model of spike initiation in neocortical pyramidal neurons. *Neuron*, 15:1427–1439, 1995.

[43] Y. Manor, J. Rinzel, I. Segev, and Y. Yarom. Low-amplitude oscillations in the inferior olive: A model based on electrical coupling of neurons with heterogeneous channel densities. *J. Neurophysiol.*, 77:2736–2752, 1997.

[44] D. Marr. A theory of cerebellar cortex. *The Journal of Physiology*, 202(437-470), 1969.

[45] L. Meng, M. A. Kramer, and U. T. Eden. A sequential monte carlo approach to estimate biophysical neural models from spikes. *J. Neural Eng.*, 8(6):065006, 2011.

[46] L. Meng, M. A. Kramer, S. J. Middleton, M. A. Whittington, and U. T. Eden. A unified approach to linking experimental, statistical and computational analysis of spike train data. *PLos ONE*, 9(1):e85269, 2014.

[47] P. Mullowney and S. Iyengar. Parameter estimation for a leaky integrate-and-fire neuronal model from isi data. *Journal of Computational Neuroscience*, 24(2):179–194, 2008.

[48] V. Nikolenko, K. E. Poskanzer, and R. Yuste. Two-photon photostimulation and imaging of neural circuits. *Nat. Meth.*, 4(11):943–950, 2007.

[49] M. Onizuka, H. Hoang, M. Kawato, I. T. Tokuda, N. Schweighofer, Y. Katori, K. Aihara, E. J. Lang, and K. Toyama. Solution to the inverse problem of estimating gap-junctional and inhibitory conductance in inferior olive neurons from spike trains by network model simulation. *Neural Networks*, 47:51–63, 2013.

[50] L. Paninski, J. Pillow, and E. Simoncelli. Maximum likelihood estimation of a stochastic integrate-and-fire neural encoding model. *Neural Computation*, 16:2533–2561, 2004.

[51] E. Pastrana. Optogenetics: Controlling cell function with light. *Nat. Meth.*, 8(1):24–25, 2010.

[52] A. A. Prinz, D. Bucher, and E. Marder. Similar network activity from disparate circuit parameters. *Nature Neuroscience*, 7:1345–1352, 2004.

[53] D. Purves, G. J. Augustine, D. Fitzpatrick, W. C. Hall, A. S. LaMantia, J. O. McNamara, and M. S. Williams. *Neuroscience*. Sinauer Associates, Inc., 2004.

[54] C. S. Quiroga-Lombard, J. Hass, and D. Durstewitz. Method for stationary segmentation of spike train data with application to the pearson cross-correlation. *Journal of Neurophysiology*, 110:562–572, 2013.

[55] M. Rapp, Y. Yarom, and I. Segev. Modeling back propagating action potential in weakly excitable dendrites of neocortical pyramidal cells. *Proceedings of the National Academy of Sciences of the United States of America*, 93:11985–11990, 1996.

[56] M. Sato. On-line model selection based on the variational bayes. *Neural Computation*, 13:1649–1681, 2001.

[57] E. D. Schutter and J. M. Bower. An active membrane model of the cerebellar purkinje cell. i. simulation of current clamps in slice. *Journal of Neurophysiology*, 71:375–400, 1994.

[58] N. Schweighofer, K. Doya, H. Fukai, J. V. Chiron, T. Furukawa, and M. Kawato. Chaos may enhance information transmission in the inferior olive. *Proceedings of the National Academy of Sciences of the United States of America*, 101:4655–4669, 2004.

[59] N. Schweighofer, K. Doya, and M. Kawato. Electrophysiological properties of inferior olive neurons: a compartmental model. *Journal of Neurophysiology*, 82(2):804–817, 1999.

[60] M. N. Shadlen and W. T. Newsome. The variable discharge of cortical neurons: Implications for connectivity, computation, and information coding. *The Journal of Neuroscience*, 18(10):3870–3896, 1998.

[61] S. Shinomoto, K. Miura, and S. Koyama. A measure of local variation of interspike intervals. *Biosystems*, 79(1-3):67–72, 2005.

[62] C. Sotelo, R. Llinas, and R. Baker. Structural study of inferior olivary nucleus of the cat: morphological correlates of electrotonic coupling. *Journal of Neurophysiology*, 37:541–559, 1974.

[63] I. T. Tokuda, C. E. Han, K. Aihara, M. Kawato, and N. Schweighofer. The role of chaotic resonance in cerebellar learning. *Neural Networks*, 23:836–842, 2010.

[64] I. T. Tokuda, H. Hoang, N. Schweighofer, and M. Kawato. Adaptive coupling of inferior olive neurons in cerebellar learning. *Neural Networks*, 47:42–50, 2013.

[65] B. Torben-Nielsen, I. Segev, and Y. Yarom. The generation of phase differences and frequency changes in a network model of inferior olive subthreshold oscillations. *PLoS Comput. Biol.*, 8(7):e1002580, 2012.

[66] I. Tsuda. Dynamics link of memory - chaotic memory map in nonequilibirum neural networks. *Neural Networks*, 5:313–326, 1992.

[67] I. Tsuda, H. Fujii, S. Todokoro, T. Yasuoka, and Y. Yamaguchi. Chaotic itinerancy as a mechanism of irregular changes between synchronization and desynchronization in a neural network. *Journal of Integrative Neuroscience*, 3:159–182, 2004.

[68] T. Tsunoda, T. Omori, H. Miyakawa, M. Okada, and T. Aonishi. Estimation of intracellular calcium ion concentration by nonlinear state space modeling and expectation maximization algorithm for parameter estimation. *Journal of the Physical Society of Japan*, 79(12):124801, 2010.

[69] I. Tyukin, E. Steur, H. Nijmeijer, D. Fairhurst, I. Song, A. Semyanov, and C. Van Leeuwen. State and parameter estimation for canonic models of neural oscillators. *International Journal of Neural Systems*, 20(3):193–207, 2010.

[70] M. Uusisaari and E. D. Schutter. The mysterious microcircuitry of the cerebellar nuclei. *The Journal of Physiology*, 589:3441–3457, 2011.

[71] M. C. Vanier and J. M. Bower. A comparative survey of automated parameter search methods for compartmental neural models. *Journal of Computational Neuroscience*, 7:149–171, 1999.

[72] Y. Wang, A. Barakat, and H. Zhou. Electrotonic coupling between pyramidal neurons in the neocortex. *PLos ONE*, 5(4):e10253, 2010.